

Effects of all-sky assimilation of GCOM-W1/AMSR2 radiances in the ECMWF system

Masahiro Kazumori¹, Alan J. Geer, and
Stephen J. English

Research Department

¹Japan Meteorological Agency

To be submitted to Quarterly Journal of the Royal Meteorological Society

September 2014

This paper has not been published and should be regarded as an Internal Report from ECMWF.

Permission to quote from it should be obtained from the ECMWF.



Series: ECMWF Technical Memoranda

A full list of ECMWF Publications can be found on our web site under:

<http://www.ecmwf.int/publications/>

Contact: library@ecmwf.int

©Copyright 2014

European Centre for Medium-Range Weather Forecasts
Shinfield Park, Reading, RG2 9AX, England

Literary and scientific copyrights belong to ECMWF and are reserved in all countries. This publication is not to be reprinted or translated in whole or in part without the written permission of the Director-General. Appropriate non-commercial use will normally be granted under the condition that reference is made to ECMWF.

The information within this publication is given in good faith and considered to be true, but ECMWF accepts no liability for error, omission and for loss or damage arising from its use.

Abstract

This paper assesses the impact of Advanced Microwave Scanning Radiometer 2 (AMSR2) radiances in the all-sky assimilation of the European Centre for Medium-Range Weather Forecasts (ECMWF). Individual impacts of three microwave imagers including AMSR2 were examined by using a baseline experiment that had no microwave imager data. The three microwave imagers brought similar improvements in humidity, temperature, and wind first guess (FG) fields in the troposphere. Improvements were found both in fits to analyses and to other observations. Moreover, significant improvements of wind and geopotential height fields in the troposphere were found in day 3 to day 6 forecasts. AMSR2 made larger improvements than other microwave imagers to geopotential height forecasts in the northern hemisphere. The addition of AMSR2 radiance data on top of the full ECMWF operational dataset gave mixed results. Consistent improvements in the FG fit to humidity observations were confirmed. However, the FG fit for several channels of the microwave temperature sounding instruments was degraded. Mean FG departure of AMSR2 shows biases in certain local time and meteorological conditions. The causes of the biases were identified as insufficient representation of cloud liquid water path (LWP) in the forecast model under unstable conditions and insufficient amplitude of LWP diurnal variation in stratocumulus areas in the tropics. The assimilation of too much biased data might start to bring negative effects for the analysis and forecasts perhaps outweighing the improvements in the assimilation. However, similar to what was found in the no-imager baseline experiments, AMSR2 brought significant improvements of the geopotential height field in the southern hemisphere lower troposphere for day 5 to day 7 forecasts.

1 Introduction

Space-based microwave imager observations have become an indispensable part of global Earth Observing System (EOS). In data assimilations for numerical weather predictions (NWP), the information obtained from the microwave imagers helps improve atmospheric humidity, cloud, and precipitation analyses and forecasts. Operational NWP centers have been utilizing these information from radiance data of the Defense Meteorological Satellite Program (DMSP) satellite Special Sensor Microwave Imager Sounder (SSMIS) (Kunkee et al., 2008, Bell et al., 2008), the Tropical Rainfall Measuring Mission (TRMM) Microwave Imager (TMI) (Kummerow et al., 1998), the Aqua Advanced Microwave Scanning Radiometer for EOS (AMSR-E) (Kawanishi et al., 2003) for their global data assimilation (Bauer et al., 2006a,b, Treadon et al., 2002), and further developments and enhancements are in progress (Bauer et al., 2011). In the European Centre for Medium-Range Weather Forecasts (ECMWF) NWP system, the microwave radiance data from SSMIS, TMI, and AMSR-E have been assimilated directly in all-sky conditions (Bauer et al., 2010, Geer et al., 2010, Geer and Bauer, 2010, 2011). In regional data assimilation, Japan Meteorological Agency's (JMA) mesoscale NWP system utilizes the microwave imager radiances in clear conditions and retrieved precipitation from the radiances are assimilated in rainy conditions (Kazumori, 2014). These papers prove the assimilation of the microwave imager data in all weather conditions can improve the accuracy of humidity and cloud analysis and also benefits forecasts.

The observation information from the microwave imagers is very valuable for today's operational NWP systems and their continuity must be ensured. Japan Aerospace Exploration Agency (JAXA) is conducting the Global Change Observation Mission (GCOM) for continued global meteorological and environmental monitoring (Imaoka et al. 2010). The GCOM project is composed of six polar orbiting satellites. The GCOM-W series are for observations of the water cycle and the GCOM-C series are for observations of climate change. Each series uses three satellites to cover a 10 to 15 years observation period. The GCOM-W1 is the first satellite of the GCOM-W series and was launched on 18 May 2012. GCOM-W1 uses an afternoon orbit with an equator crossing time (ascending) at approximately 1:30 pm local time, which makes it part of the A-train, the Earth observation satellite constellation managed by the National

Aeronautics and Space Administration (NASA).

GCOM-W1 uses an Advanced Microwave Scanning Radiometer 2 (AMSR2) (JAXA, 2013) for observations of microwave radiances from the Earth. AMSR2 is the successor of the Advanced Microwave Scanning Radiometer (AMSR) on the Advanced Earth Observing Satellite II (ADEOS-II) and AMSR-E on the Aqua satellite. Scientific observations of AMSR2 began on 3 July 2012 and real time data distribution was started in May 2013. The AMSR2 radiance data are available from July 2012 to the present. AMSR2 should take over the role of AMSR-E in Earth observing system. JMA started using AMSR2 radiance data in their NWP systems on 12 September 2013 (Kazumori and Egawa, 2014). The assimilation in the JMA global NWP system is limited to clear scene data. The JMA mesoscale NWP system assimilates the clear sky radiances and retrieved precipitation. They showed similar positive impacts on the humidity analysis and precipitation forecasts to those from AMSR-E. However, AMSR2 radiance data quality and benefits in global data assimilation have not yet been investigated with an all-sky radiance assimilation scheme. Hence in this paper, we assess the quality and impact of all-sky AMSR2 radiance data in the ECMWF system. We perform two kinds of experiments. The first is a study on the individual impacts of three microwave imagers (AMSR2, SSMIS, and TMI) on top of a baseline experiment that has no microwave imager data. The second looks at the addition of AMSR2 data on the top of the full ECMWF operational observation set that includes SSMIS and TMI observations. In section 2, all-sky radiance assimilation in the ECMWF system, AMSR2 radiance data, setting of observation errors, and quality controls are described. In section 3, assessments of AMSR2 radiance data quality are provided. The data assimilation experiments using AMSR2 and their results are provided in section 4. Finally, section 5 presents discussion and conclusion.

2 Methodology

2.1 All-sky assimilation in the ECMWF system

In the ECMWF system, all-sky radiance assimilation (Bauer et al., 2010, Geer et al., 2010, Geer and Bauer, 2010, 2011) was introduced for the microwave imagers in 2009. At present, SSMIS and TMI observations are assimilated over oceans. Assimilation of SSMIS 183 GHz water vapor sounding channels was started in cycle 39r1 (Geer, 2013) together with improvements of snow-scattering radiative transfer calculations (Geer and Baordo, 2014). In the all-sky approach, microwave imager radiances are used in a 12 hour assimilation window with a four dimensional variational (4D-Var) scheme in clear, cloudy and precipitating situations over the oceans to improve the analysis and forecast. Benefits from the assimilation are found not only in water vapor, cloud, and precipitation but also in wind and geopotential height forecasts. The benefits to the forecasts are thought to come from both from improved instantaneous analysis and 4D-Var tracing effects on water vapor, cloud, and precipitation features, where even in the presence of relatively large forecast model errors and observation operator errors, there is still information content to be gained (English et al., 2013).

The present assimilation of microwave imagers is not optimal in many ways. Major issues include 1) Inter-channel observation error correlations are much stronger in cloud than in clear skies for microwave imager radiances (Bormann et al., 2011). These are not yet modeled. 2) There is no control variable for cloud or precipitation. The control variables are the usual cloud-free atmospheric variables, i.e. transformations of wind, temperature, surface pressure and specific humidity. Though clouds and precipitation are not part of the control vector, they are still analyzed implicitly, being generated by the cloud physics of the forward model used within 4D-Var. 3) The presence of the forecast model biases in the cloud

physics can produce unnecessary analysis increments in the assimilation. We will explore this final issue in depth in the current paper.

To make use of the radiances in the variational data assimilation, a fast radiative transfer model for transforming analysis variables into radiance space (the forward model), and its adjoint model are required. In the ECMWF system, the Radiative Transfer for the Television Infrared Observation Vertical Sounder (RTTOV; Saunders et al., 1999) is utilized. The RTTOV-SCATT component of RTTOV is employed for cloud and precipitation radiative transfer. RTTOV-SCATT is a fast model designed for assimilating microwave radiances in all-sky conditions (Bauer et al., 2006). The radiative transfer equation is solved using the delta-Eddington approach (Joseph et al., 1976). Transmittances for oxygen and water vapor are computed from regression tables driven by atmospheric predictors, just as in the normal RTTOV. Bulk optical properties for cloud water, cloud ice, rain, and snow are taken from look-up-tables. At the time of this study, cycle 40r1 was the operational version of the ECMWF system and RTTOV version 10 (Saunders et al., 2010) was employed for the radiative transfer calculation (Bormann et al., 2011). For the calculation of the microwave imager's radiance, atmospheric profiles (i.e. temperature, water vapor, ozone, cloud liquid water, cloud ice water, rain water, and snow) from the model are used for inputs. The all-sky radiances are computed as the weighted average of the radiance from two independent sub-columns, one clear and one cloudy. The weighting is determined according to the effective cloud fraction of Geer et al. (2009), which approximates sub-grid cloud and precipitation variability. Moreover, surface properties (e.g. temperature and surface wind) from the model are used for calculations of microwave ocean surface emissivity using the FAST microwave Emissivity Model version 5 (FASTEM-5) (Liu et al., 2011, Bormann et al., 2012). The azimuth variation of oceanic microwave radiances is of order 2 K at higher surface wind speeds and ideally this effect should be modeled (Kazumori and English, 2014). However, because azimuth angle information on SSMIS and TMI is not provided with the real time data, the azimuth component of the FASTEM-5 was not utilized for any microwave imager (SSMIS, TMI, and AMSR2) in these experiments.

2.2 AMSR2 data

AMSR-E stopped normal observation on 4 October 2011 and now operates with a slow rotation mode for limited inter-calibration with AMSR2. However, scientific observations from AMSR-E are no longer available. AMSR2 is the only microwave imager in the A-Train orbit and no other microwave imager in the same orbit is planned, so it is expected to fill a temporal and spatial gap in coverage and hence its assimilation should bring improvements in analyses and forecasts.

AMSR2 has several advantages compared to AMSR-E. AMSR2 level 1b radiance data have a wider swath (approximately 1618 km width for AMSR2, 1458 km for AMSR-E) because 243 instantaneous fields of views (IFOV) per scan are available in AMSR2, whereas AMSR-E IFOV number was 196. AMSR2 data have an improved horizontal resolution because the main reflector size of AMSR2 (2.0 m) is increased from that of AMSR-E (1.6 m) (JAXA, 2013). Moreover, AMSR2 has channels at both 6.925 GHz and 7.3 GHz to mitigate radio frequency interference (RFI). AMSR2 covers the spectral range from 6.925 GHz to 89.0 GHz.

A further advantage of AMSR2 is better calibration. The warm calibration target (hot load) has been improved, based on lessons learned from the AMSR-E hot load issues. Hence instrument origin biases (e.g. seasonal change of solar radiation intrusions to the calibration target) are reduced and smaller than those of AMSR-E (Kasahara et al. 2012). AMSR2 radiance data used in this study is level 1b brightness temperature (version 1.10) and obtained from JAXA.

Selected microwave imager channels for the assimilation in this study are summarized in Table 1 with actively assimilated channels in bold. As mentioned previously, only SSMIS and TMI are assimilated operationally at this time. Hereafter, the notations defined in Table 1 are used to specify microwave imager channels.

Table 1: Microwave imager channels (channels in bold indicate assimilated channels)

Sensor Name			AMSR2		TMI		SSMIS	
Band	Notation	Polarization	Ch#	Frequency	Ch#	Frequency	Ch#	Frequency
C	06V	V	1	6.925				
	06H	H	2	6.925				
	07V	V	3	7.3				
	07H	H	4	7.3				
X	10V	V	5	10.65	1	10.65		
	10H	H	6	10.65	2	10.65		
Ku	19V	V	7	18.7	3	19.35	13	19.35
	19H	H	8	18.7	4	19.35	12	19.35
K	23V	V	9	23.8	5	21.3	14	22.235
	23H	H	10	23.8				
Ka	37V	V	11	36.5	6	37	16	37
	37H	H	12	36.5	7	37	15	37
W	89V	V	13	89.0	8	85.5	17	91.655
	89H	H	14	89.0	9	85.5	18	91.655

2.3 Setting of observation errors

Definitions of observation error in data assimilation systems are one of the most important elements of the data assimilation system. In the all-sky assimilation of microwave imager radiances, the observation errors are defined based on a symmetric predictor sensitive to the cloud liquid water amount in 37 GHz observed and simulated radiances (Geer and Bauer, 2010, 2011). The microwave imager observations are averaged in grid boxes of approximately 80 km by 80 km to bring the horizontal scales of observed cloud and precipitation signals closer to the effective resolution of the forecast model.

For the estimation of the observation error model for AMSR2, the averaged observed radiances and simulated radiances were produced in the ECMWF system at a horizontal resolution T511 (with a 39 km grid) L137 (with 137 vertical levels) compared to operational resolution in November 2013 of T1279 (with a 16 km grid) L137. FG departures (i.e., the difference of the observed and simulated radiance) are stratified according to the symmetric cloud amount (\overline{C}_{37}) and standard deviations in the each category are calculated. The symmetric cloud amount \overline{C}_{37} is defined as follows,

$$\overline{C}_{37} = \frac{C_{37}^b + C_{37}^o}{2}. \quad (1)$$

C_{37}^b and C_{37}^o are computed from the FG and observed radiances individually by using following equation.

$$C_{37} = 1 - P_{37}, \quad (2)$$

$$P_{37} = \frac{T^v - T^h}{T_{\text{clr}}^v - T_{\text{clr}}^h} \approx \tau_{\text{CLD}}^2, \quad (3)$$

where T^v and T^h are observed (or simulated) AMSR2 radiances at 37 GHz. T_{clr}^v and T_{clr}^h are simulated radiances from the same profiles but without clouds or precipitation. P_{37} is the normalized polarization difference (Petty and Katsaros, 1990, Petty, 1994, Geer and Bauer, 2011), and under some rather severe assumptions, P_{37} is approximately equal to the square of the surface to space cloud and precipitation transmittance τ_{CLD} . P_{37} goes to zero under heavy cloud (precipitation) and C_{37} goes to unity. P_{37} goes to unity under clear situation and C_{37} goes to zero. Figure 1 shows mean and standard deviation of FG departures as functions of C_{37} for 6, 19, and 37 GHz vertical polarized channels. The statistics are calculated from one month AMSR2 data (August 2012). Geer and Bauer (2010, 2011) have complete descriptions of the definition of the observation error in all-sky assimilation. The FG departure variances can be expressed as follows,

$$t^2 = r^2 + b^2, \quad (4)$$

where t , r , and b are total, observation, and background error standard deviations (Desroziers et al., 2005). The background error is assumed as 1.0 K for all microwave imager channels in the all-sky radiance assimilation. Estimated parameters to define the total error for all AMSR2 channels are summarized in Table 2. Figure 1 shows the total errors used for the assimilation with red lines. Dotted red lines in the middle right panel in Figure 1 show the definition of the parameters (t_{CLR} , t_{CLD} , C_{CLR} , and C_{CLD}).

Table 2: Parameters for the observation error model of AMSR2

AMSR2	Frequency (GHz)	t_{CLR}	t_{CLD}	C_{CLR}	C_{CLD}
	and polarization				
	06V	1.5	6.2	0.03	0.48
	06H	2.0	12.0	0.03	0.48
	07V	1.5	6.8	0.03	0.48
	07H	2.0	13.5	0.03	0.48
	10V	2.0	13.5	0.03	0.48
	10H	3.0	26.5	0.03	0.48
	19V	2.0	18.5	0.00	0.48
	19H	4.0	37.0	0.00	0.48
	23V	2.5	10.5	0.00	0.46
	23H	4.5	22.0	0.00	0.46
	37V	2.2	17.8	0.00	0.46
	37H	4.0	39.0	0.00	0.46
	89V	2.4	15.2	0.00	0.45
	89H	4.5	14.0	0.00	0.13

2.4 Quality control of AMSR2 radiances

In prescreening step for AMSR2 data in the ECMWF system, unphysical values of the radiance data, the data in surface temperature less than 274 K and land or sea ice contaminated data are removed before the assimilation. The data in high latitudes (latitude poleward of 60 degrees north or poleward of 60 degrees

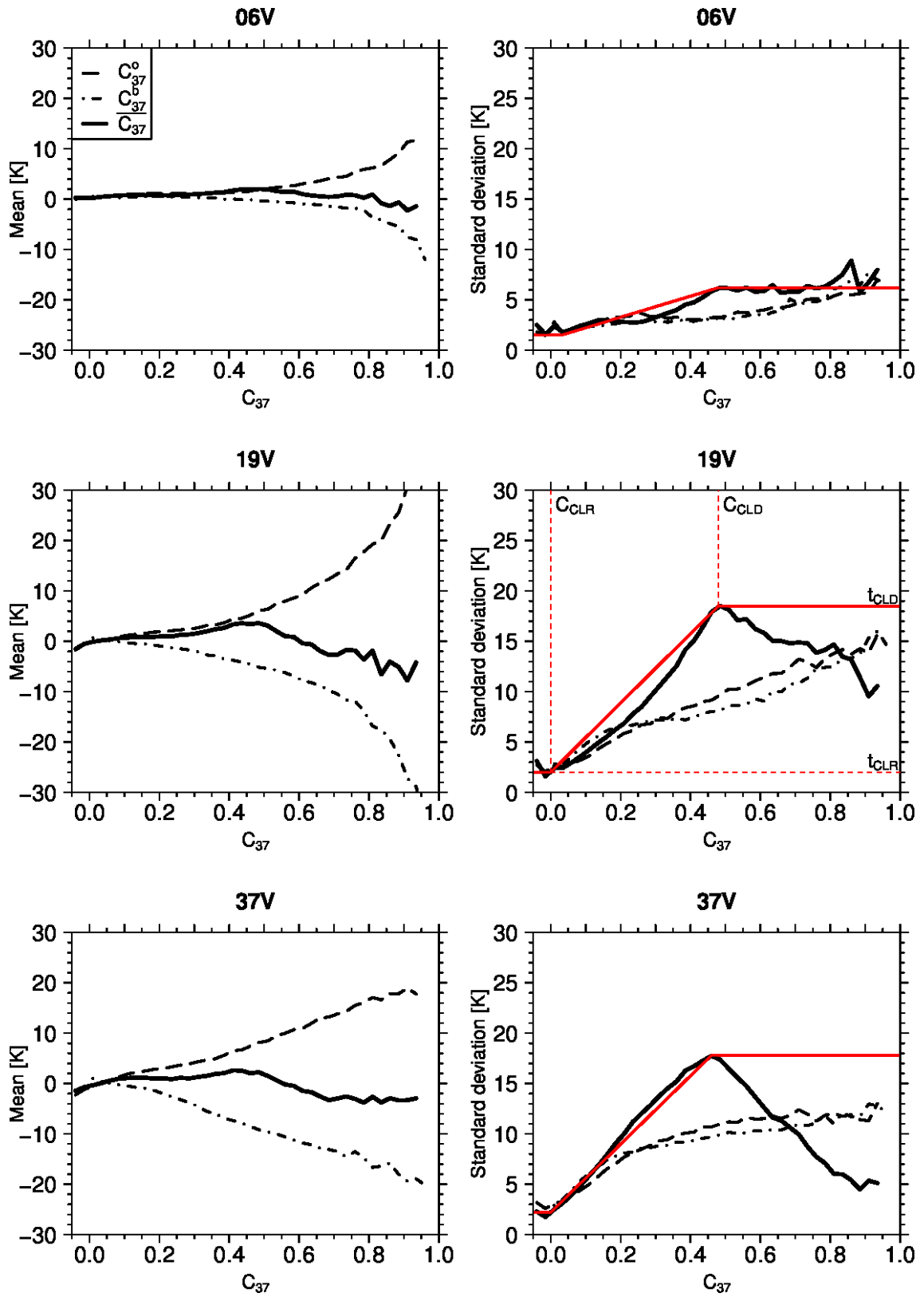


Figure 1: Mean (left panels) and standard deviation (right panels) of AMSR2 FG departure for 6 GHz V (top), 19 GHz V (middle), and 37 GHz V (bottom) as a function of symmetric cloud amount C_{37} . Red lines indicate defined total errors. Dotted red lines in the middle right panel show the definition of the parameters (t_{CLR} , t_{CLD} , C_{CLR} , and C_{CLD}).

south) are not used. Background checks are performed based on normalized FG departures with the total error (Järvinen and Undén, 1997). Observations are rejected when

$$\frac{d}{\sqrt{r^2 + b^2}} \equiv \frac{d}{t} > \delta, \quad (5)$$

where d is the bias corrected FG departure and, for all-sky observations, t is the total error from the symmetric error model. δ is set to 2.5 for all-sky observations.

Moreover, biased data in cold sectors are rejected. The cold sector biases have been known as positively biased FG departure (approximately 5 to 10 K) in microwave imager observations in the ECMWF system (Geer et al., 2009, Geer and Bauer 2010, 2011). The biased data are rejected based on the following three criteria:

$$\text{TCWV} < 15 \text{ kg m}^{-2}, \quad (6)$$

$$\frac{\text{LWP}}{\text{LWP} + \text{IWP}} > 0.5, \quad (7)$$

$$\text{LWP} + \text{IWP} + \text{RWP} + \text{SWP} > 0.01 \text{ kg m}^{-2}. \quad (8)$$

Total column water vapor (TCWV), cloud liquid water path (LWP), and cloud ice water path (IWP), rain and snow water paths (RWP, SWP) are taken from the FG model fields. Furthermore, in cycle 37r3 in the ECMWF system (introduced in September 2011) another criterion was added to avoid areas where the assimilation system had started to generate large spurious negative temperature increments. These occurred very occasionally at high latitudes with near-zero TCWV in the model, where the assimilation system could only decrease the modeled brightness temperatures by reducing atmospheric temperature itself. Due to the severity of the problem, a very cautious rejection criterion was applied:

$$\text{TCWV} < 8 \text{ kg m}^{-2}. \quad (9)$$

The problem was triggered by a model change to supersaturation and deposition rate for clouds, intended to fix a winter 2 meter temperature forecast bias in Europe. However, as a side effect, there was an increase of the cloud liquid water in frontal areas (these biases will be evident in the following results) and, the trigger for the assimilation difficulties, a change to cloud amounts in cold-air outbreak regions and hence a change in the microwave imager bias characteristics in high latitudes.

Finally, variational quality control (VarQC: Ingleby and Lorenc, 1993; Andersson and Järvinen, 1998) is applied through minimization in the 4D-Var for all-sky observations as well as most of other observations. VarQC applies weights to the observations. VarQC adaptively decreases the weight of the observations when they are significant outliers from the analysis.

3 Data quality assessment

Data quality assessment is performed based on the FG departure statistics. Figure 2 shows FG departure biases and standard deviations for the three microwave imagers, without any bias correction, for July

2013. It is clear that there are inter-instrument biases. Absolute calibrations of the microwave imagers are different from sensor to sensor, though the differences are mostly characterized by a constant offset rather than any scene dependence. These kinds of biases are corrected in the assimilation system using a variational bias correction scheme (VarBC, Dee 2004). The three microwave imagers show comparable standard deviations. This indicates noise levels in the observations are similar. Statistics for other months showed similar results. The seasonal variation is minimal for AMSR2. In these global ocean data statistics, AMSR2 radiance data quality is comparable to other microwave imagers.

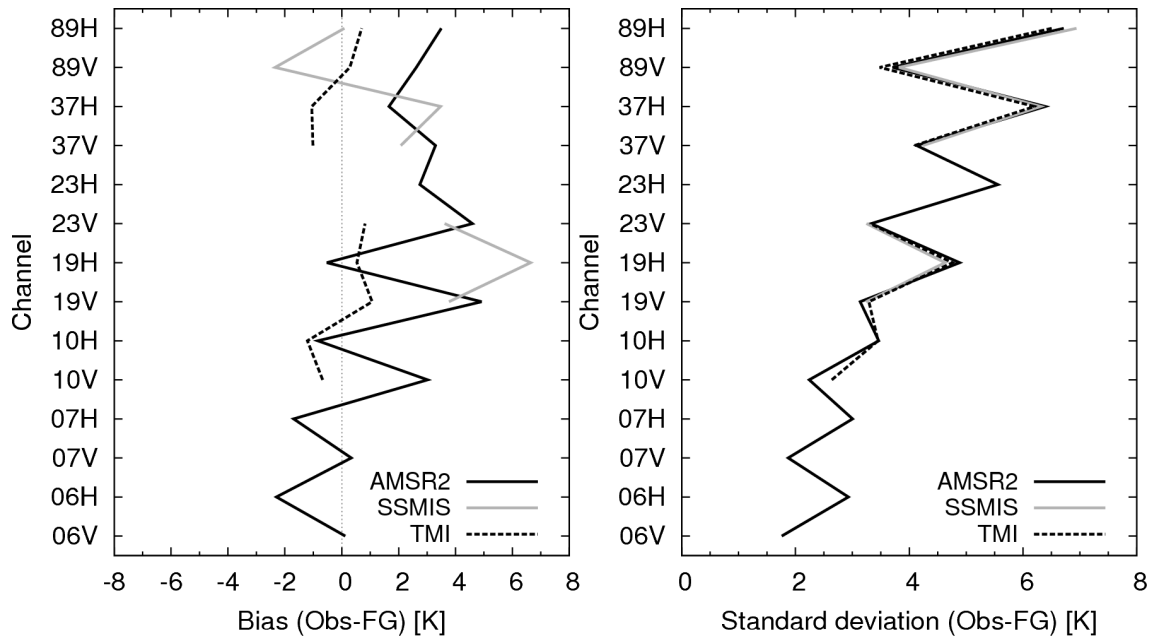


Figure 2: Mean biases (observed minus FG radiances) for AMSR2, SSMIS, and TMI. The period is for July 2013.

AMSR2 has low frequency channels (6, 7, and 10 GHz). Although these channels are not used in the atmospheric analysis in the ECMWF system, the data quality assessment was performed for those channels, with a view to future use of this data. The low frequency channels are affected by sun glint in some areas. Figure 3 shows the ascending orbit and descending orbit FG departure distribution of 06V on 1 August 2012. In the southern hemisphere ascending orbit, approximately 3 to 6 K positive biased areas exist in each swath for the low frequency channels. (c) and (d) shows the corresponding sun glint angle for AMSR2. These positive biases vary seasonally depending on the solar position, but the variation is predictable. The biased data could be rejected with a condition of the sun glint angle less than 25 degrees.

No sun glint effect was found in the selected channels for the assimilation (from 19 to 89 GHz). However, for the low frequency horizontal channels, large negative biases in FG departure were found. The biases showed negative correlations to surface wind speed. This performance is similar to a result obtained from FASTEM-1 case (Kazumori et al. 2008). Moreover, Geer and Baordo (2014) shows that biases in 10 GHz FG departures from TMI observations are quite large compared to the signal in these channels. The biases are 40 % of the standard deviation of the FG departure, as opposed to about 20 % in most other channels; the large uncorrected biases are one main reason preventing operational assimilation of the low frequency channels. Much more work would be required to investigate the cause of the biases.

Furthermore, some RFI contaminated data was found in the low frequency channels. One of the main

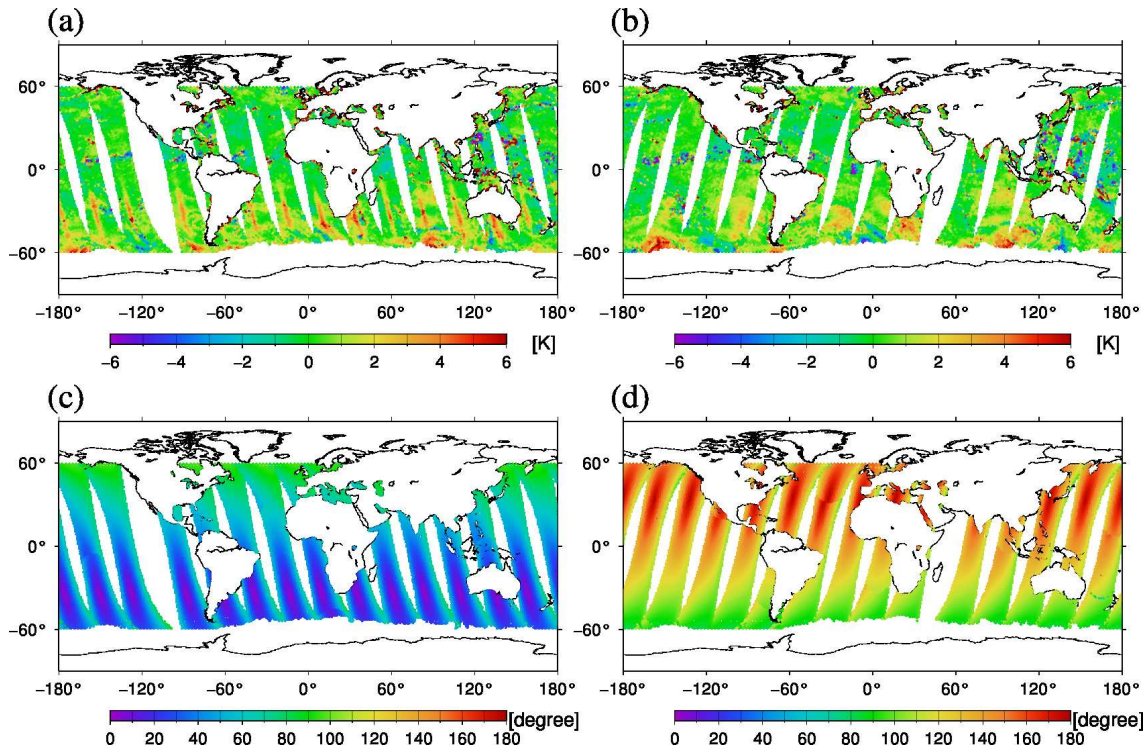


Figure 3: AMSR2 6 GHz V FG departures in ascending orbit (a) and descending orbit (b) in 1 August 2012. (c) and (d) are estimated sun glint angle for ascending and descending orbits, respectively.

sources is reflected microwave signals from geostationary satellites. In AMSR2 19 GHz channels, RFI contamination was found in the coast line of the United States. Figure 4 shows the mean FG departure at 19 GHz vertical polarization for ocean data before and after the prescreening. The result shows that prescreening with the symmetric observation error model (Eq. (5)) can reject most of the RFI contaminated data effectively. Except for the RFI contaminated data, instrument origin biases were not identified in AMSR2 FG departure statistics. SSMIS has clear orbit dependent biases in 89V. Mean descending SSMIS FG departure biases in 89V were approximately 0.7 K higher than that of ascending data. The case in AMSR2 was less than 0.2 K in global average.

4 Data assimilation experiments

We perform two kinds of data assimilation experiments. The first is a study on individual impacts of three microwave imagers (AMSR2, SSMIS, and TMI) by using a baseline experiment that has no microwave imager data. In the ECMWF system (cycle 40r1), the microwave imagers SSMIS and TMI are already used operationally. Addition of a new microwave imager observation (i.e. AMSR2) on top of these existing instruments shows less additional benefit because the system already has similar observations. These individual impact experiments are the fairest way to compare the different sensors. The second kind of experiment is an impact study of AMSR2 on top of the full ECMWF operational observation dataset, including SSMIS and TMI imager observations. This shows the incremental benefit of AMSR2 and is the basis of the decision whether or not to begin assimilating it operationally in the ECMWF system.

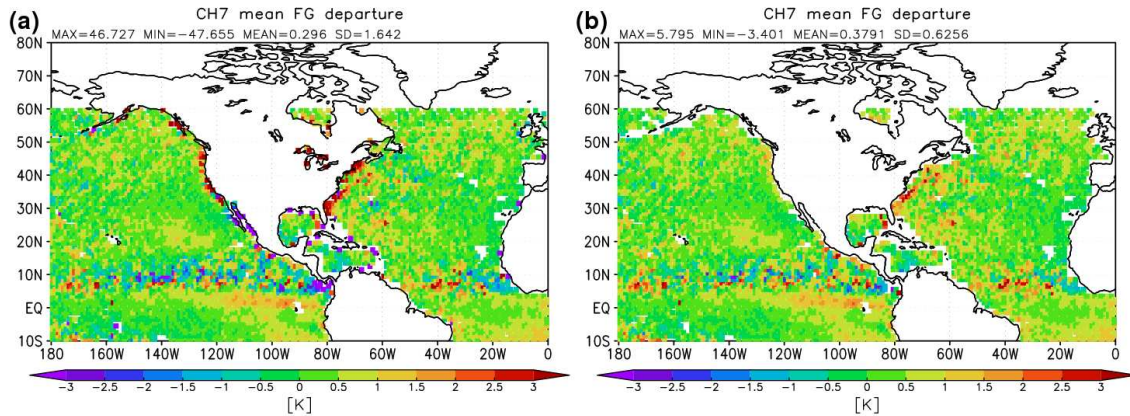


Figure 4: Mean AMSR2 19 GHz V FG departure distributions from 15 July to 15 October, 2013. (a) all ocean data, (b) prescreened data.

In order to reduce computational costs and to be able to run long term experiments with statistically significant results, the T511L137 system of ECMWF cycle 40r1 was used. Although the horizontal resolution is approximately half of the ECMWF operational system, general characteristics of the impact of the microwave imager assimilation are similar to the operational system. Two periods were selected. One is from 1 January to 1 May 2013 including boreal winter, and the other is from 15 June to 15 October 2013 including boreal summer. The observations from AMSR2, SSMIS (F17), TMI are available for both periods. The first month of each period was removed from the evaluations to allow to AMSR2 VarBC coefficients to spin up. The combined six month period from 1 February to 1 May and from 15 July to 15 October, 2013 was used for evaluation. Forecasts were performed every day at 00 UTC and 12 UTC. AMSR2 channel selection follows that of other microwave imagers in the ECMWF system. The selected AMSR2 channels for the assimilation are 19V, 19H, 23V, 23H, 37V, and 89V. Other channels (e.g. lower frequencies, higher frequency H-pol channels) tend to show larger biases in comparison to the useful atmospheric signal, as revealed in our data assessment for AMSR2.

4.1 Experiment for the impact study of each microwave imagers

4.1.1 Design of the experiment

In the Baseline run, the assimilation of all microwave imager channels was turned off. That is, the Baseline experiments contain the full operational observing system except for the microwave imager channels. In Test 1, AMSR2 radiance data are added to the Baseline. In Test 2, SSMIS F17 data are added to the Baseline. In Test 3, TMI data are added to the Baseline. Other observation data usage, data prescreening, the radiative transfer model, forecast model are same. SSMIS humidity sounding data are assimilated in all-sky approach (Geer, 2013) for all runs. For AMSR2, a 23 GHz H channel is available (other microwave imagers do not have the corresponding channel) and used in the Test 1. The experiment configurations are summarized in Table 3.

Table 3: Experiment configuration

Experiment Name	Description and used microwave imager channels
Baseline	ECMWF cycle 40r1 (T511L137 resolution) - minus all microwave imager channels
Test1	Baseline plus AMSR2 (19V, 19H, 23V, 23H, 37V, 89V)
Test2	Baseline plus SSMIS F17 (19V, 19H, 23V, 37V, 89V)
Test3	Baseline plus TMI (19V, 19H, 23V, 37V, 89V)

Table 4: Experiment configuration

Experiment Name	Description and used microwave imager channels
Control	ECMWF cycle 40r1 as of November 2013. The resolution is T511L137
Test	Control plus AMSR2 (19V, 19H, 23V, 23H, 37V, 89V)

4.1.2 FG departure statistics

To confirm the impact on short range forecasts in the data assimilation experiment, the FG fit to other observations is examined. The departures from the FG are calculated after the bias correction. Figure 5 shows the fit to Microwave Humidity Sounder (MHS) and Advanced Microwave Sounding Unit-A (AMSUA) observations. Reductions of standard deviation of the FG departure in MHS channel 4 and 5 (lower tropospheric humidity sensitive channels) were confirmed globally. Similar improvements for Advanced Technology Microwave Sounder (ATMS) channels 18 to 22 were found. As for AMSUA-A, improvements in channel 5 were found globally. However, degradations of the fits in channel 9 and channel 6 (northern and southern hemisphere) were found. Figure 6 shows results for radiosonde observation (RAOB) temperature, specific humidity, in-situ wind observations, and Atmospheric Motion Vector (AMV) observations. These results show improvements in the lower tropospheric wind and humidity field. Although RAOB temperature shows neutral results, other observations (Infra-red satellite radiances, GPSRO) show consistent improvements in lower tropospheric fields. All these results are common among the three microwave imagers and the results indicate that the assimilation of any of these microwave imagers can bring substantial benefit to the accuracy of the short range forecast field in humidity, temperature, and wind.

4.1.3 Impacts on analysis and forecast fields

Figure 7 shows forecast scores for vector wind for various forecast times (from T+12 to T+216). Left column shows the score for the Test 1 (AMSR2), middle column is the Test 2 (SSMIS), and right column 10 is the Test 3 (TMI). From top row, 12, 24, 72, 120 hour forecasts are shown. The scores are the normalized difference in RMS error between these test runs and the Baseline. Negative values (blue colors) indicate a reduction in RMS error and an improvement compared to the Baseline. The own analyses are used as the reference and the normalization is performed against the Baseline. Cross hatching indicates changes at a significance level of about 95 %. The method of the RMS error calculation and the statistical significance of the difference are described in Geer et al. (2010).

In the all-sky radiance assimilation of microwave imager channels, large changes in the short range forecasts (from T+12 to T+24) were found. Because the assimilation time window is 12 hour, and verification is done against the experiment's own analysis, the results in T+12 show the normalized change of the

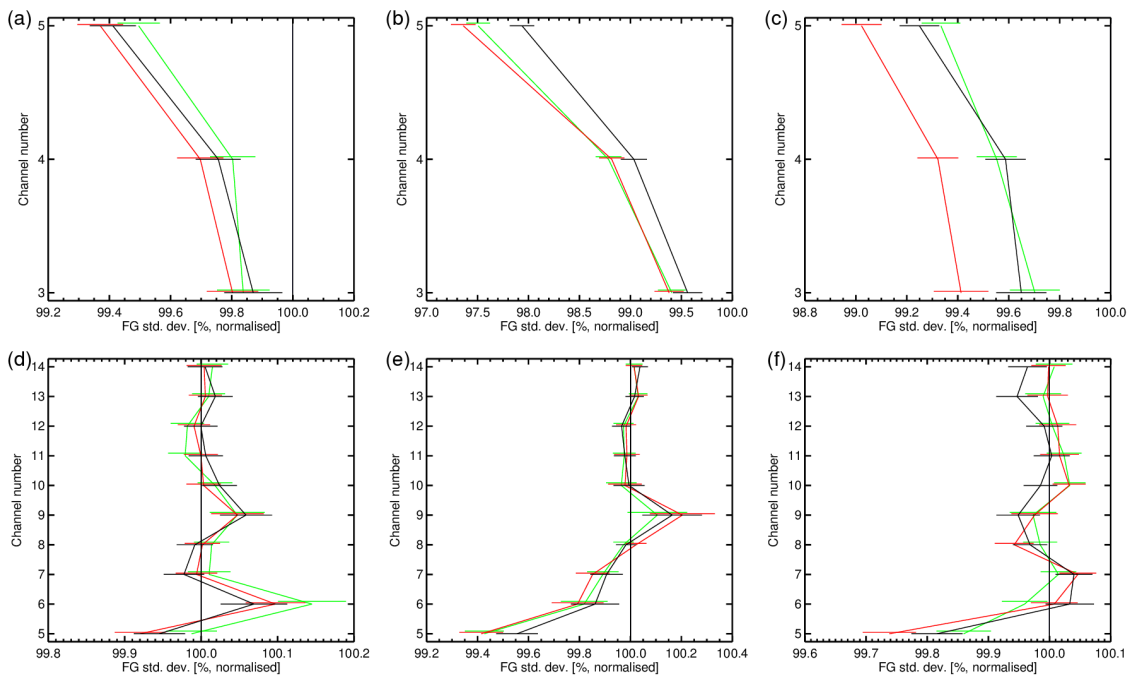


Figure 5: Normalized differences of the standard deviations of the FG departures in percentages. The normalization was performed against the Baseline results. Top panels are for MHS observations. (a) Northern hemisphere, (b) Tropics, and (c) Southern Hemisphere. Bottom panels are for AMSU-A observations. (d) Northern hemisphere, (e) Tropics, and (f) Southern Hemisphere. Vertical axes indicate channel number. Black lines are Test 1 (AMSR2), red lines are Test 2 (SSMIS F17), and green lines are Test 3 (TMI). The error bars indicate a 95 % statistical confidence interval.

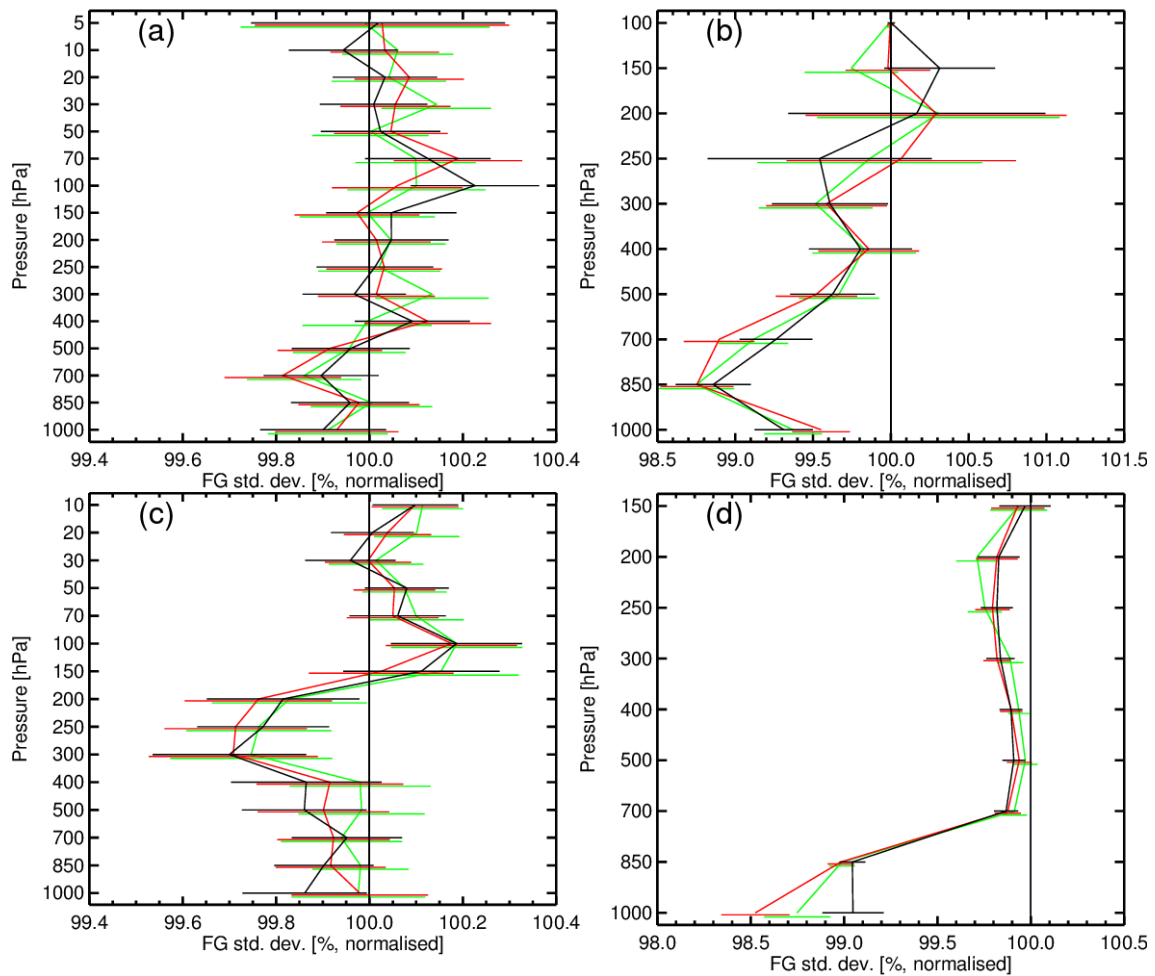


Figure 6: Same as Figure 5 but for radiosonde observations temperature (a), specific humidity (b), in-situ wind observations (East-west component) (c), and AMV (d) with vertical axis as pressure level [hPa]. The units of vertical axes are pressure level [hPa].

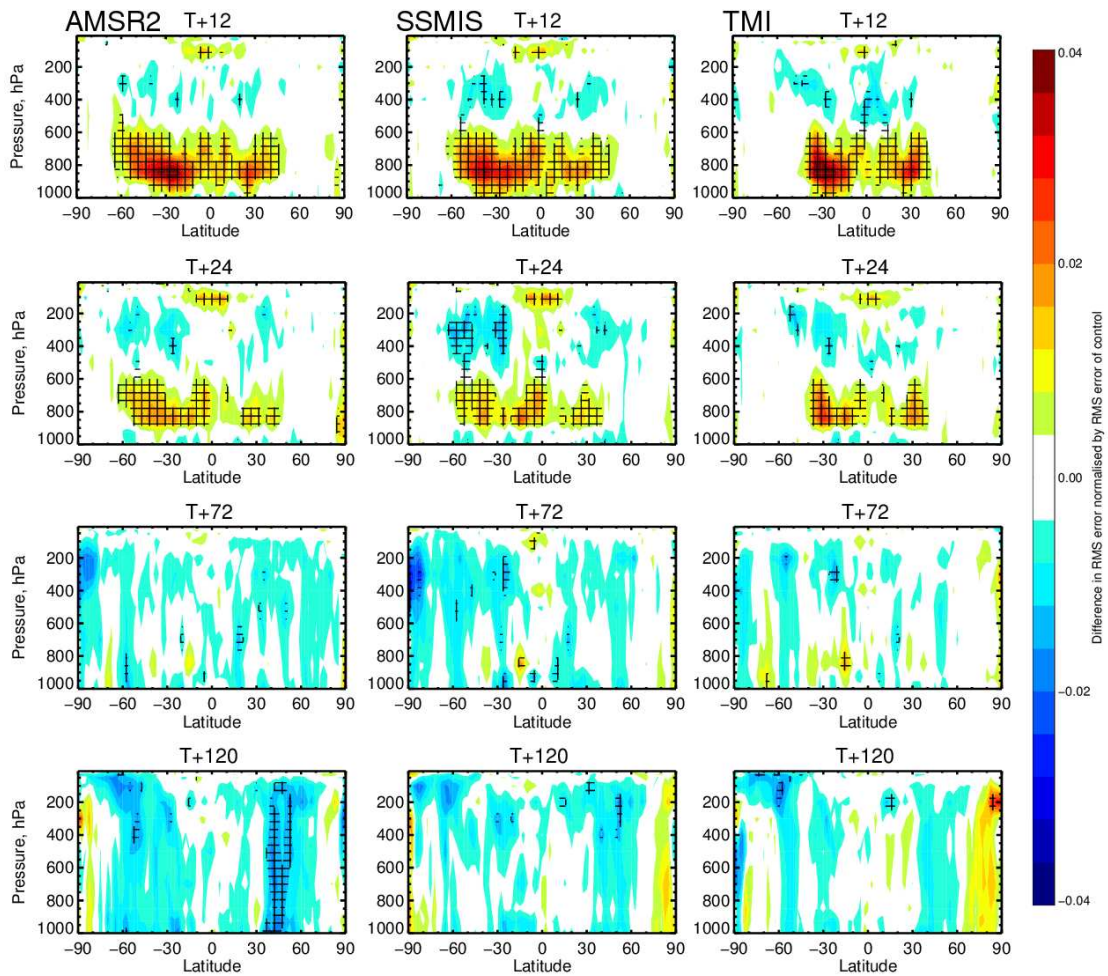


Figure 7: Normalized change in the RMS of vector wind forecast error between Test and Baseline. Left column is AMSR2, middle column is SSMIS and right column is TMI. Blue areas indicate reduced RMS forecast errors and hence improved forecast; green/yellow/red areas indicate the opposite. Cross-hatched areas show changes that are significant at the 95 % confidence interval.

RMS of the analysis increments, rather than a true measure of forecast skill. The large changes in the short range forecast were found not only for vector wind but also for relative humidity, temperature, and geopotential height field. In lower troposphere below 600 hPa, the changes are significant and resemble degradations. As shown later in Figure 12, the areas are over oceans where the microwave imager observations are assimilated. The assimilation of microwave imager radiances provides new observational information, leading to larger increments and more activity in the analysis fields, so the increases in T+12 and T+24 RMS scores are most likely a natural result of this, rather than a true increase in forecast error. The observation fits clearly demonstrate that T+12 forecasts are improved, not degraded at lower levels (section 4.1.2, improvements in AMSU-A channel 5, lower troposphere wind from AMV).

The change in RMS error is largest at the beginning of the forecast range and then decreases with time. After the 48 hour forecast, the change becomes a significant improvement. Although Figure 7 right column (Test 3, TMI assimilation) shows smaller impacts than others (TMI data coverage is limited), general characteristics of the microwave imager impacts are similar among three instruments. The left column in Figure 7 indicates that AMSR2 assimilation brings significant improvements in the vector wind field in troposphere in mid latitudes at 120 hour forecast time. The center column in Figure 7 shows that SSMIS imager assimilation brings significant improvements in the wind field in upper troposphere (200 - 400 hPa) in the southern hemisphere in the 48 hour forecast. Figure 8 shows the change of RMS errors of the geopotential height forecast against own analysis for 500 hPa as function of the forecast time. For day 3 to day 7 forecast ranges, significant improvements were confirmed in the lower troposphere in the northern and southern hemisphere for AMSR2 and SSMIS. In the northern hemisphere, improvements from AMSR2 were the largest (approximately 1 % improvement) in the day 5 forecast of the geopotential height.

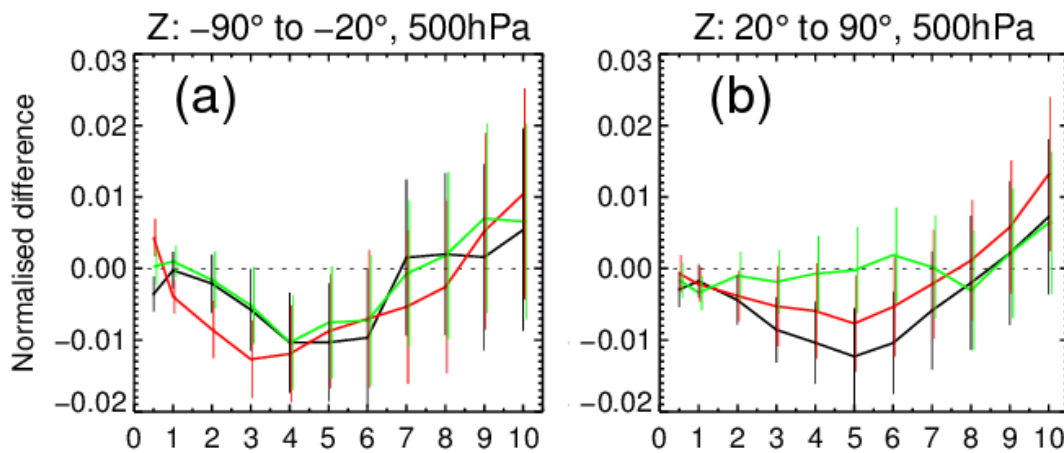


Figure 8: Normalized change in RMS forecast error in geopotential height at 500 hPa for the southern hemisphere (a), and northern hemisphere (b). Horizontal axes indicate forecast day. Verification is against own analysis. Black is Test 1 (AMSR2), red is Test 2 (SSMIS), and green is Test 3 (TMI). The error bars indicate a 95 % statistical confidence interval.

4.2 Experiment for impact study of AMSR2 radiances

4.2.1 Design of the experiment

In order to evaluate the benefit of AMSR2 radiance addition on top of all observations used in the ECMWF operational system as of November 2013, AMSR2 radiance data is added in Test run. The control run has no AMSR2 radiance data so it is the same configuration as the operational ECMWF system at cycle 40r1, except for the horizontal resolution. Again, T511L137 version was used. The experiment configurations are summarized in Table 4.

4.2.2 FG departure statistics

Figure 9 shows the statistics of SSMIS, MHS, and AMSU-A FG departures. The results show improved FG fit for SSMIS imager channels globally, as would be expected from a sensor with similar characteristics to the new AMSR2 data. Most significantly improved channels are 23 GHz V, near the water vapor absorption line. We found approximately 2 % significant improvements of the FG fit in the southern hemisphere. Because the quality controls of SSMIS are common for the both run, the results indicate that the FG field improved with AMSR2 observations. The results of MHS and AMSU-A (the advantages and disadvantages) were similar to those of in the experiment for the impact study of individual microwave imagers (section 4.1). RAOB specific humidity results showed improvements in the FG fit. Although RAOB wind showed an improvement in upper troposphere winds (jet level winds, 250 hPa), AIREP wind and AMV wind showed degradations at 200 and 150 hPa. Considering their data coverage, it could indicate the degradations occur in the upper troposphere wind over oceans. Below 850 hPa, improvements of wind fields were confirmed from RAOB wind and AMV wind as the results in section 4.1. Increases of used data count (quality control passed data) of most of the radiance data were confirmed (e.g. approximately 0.2 % increases for SSMIS) in the Test.

4.2.3 Impacts on analysis and forecast field

Figure 10 shows the normalized change in RMS error between Test and Control in vector wind field. The verification reference is in each case the experiment's own analysis. They show similar impacts to those of section 4.1 AMSR2 case (Figure 7). However, the degree of the improvement is reduced. The impacts at day 2 and day 3 become almost neutral. However, the day 5 to day 7 results still show an improvement in the troposphere in the southern hemisphere, though on this figure they are not significant. Figure 11 shows the change of RMS error of geopotential height for 500 hPa as function of forecast time. The impact on the northern hemisphere has become almost neutral. However, for day 5 to day 7 forecast ranges, the improvements in the southern hemisphere as a whole achieve statistical significance. The impact of AMSR2 is approximately 1 % improvement in the day 6 forecast of the 500 hPa geopotential height. The day 5 to day 7 scores are also supported by verification against radiosonde observations. Generally, the results of the improved FG fit to the observations suggest that the lower tropospheric humidity and wind field are improved by AMSR2 radiance assimilation. Because AMSR2 radiances were added over oceans, the impacts could be larger in oceanic areas and smaller in land areas.

Figure 12 shows maps of the RMS error difference in the 12 hour forecast at 850 hPa, for the addition of AMSR2 in the full observing system (Test) and on top of the no-imager baseline (Test1). In the former, the normalized change of relative humidity RMS errors is much smaller (compare Figure 12 (b) to (a)). This is because SSMIS and TMI data are already assimilated in the Control run and the

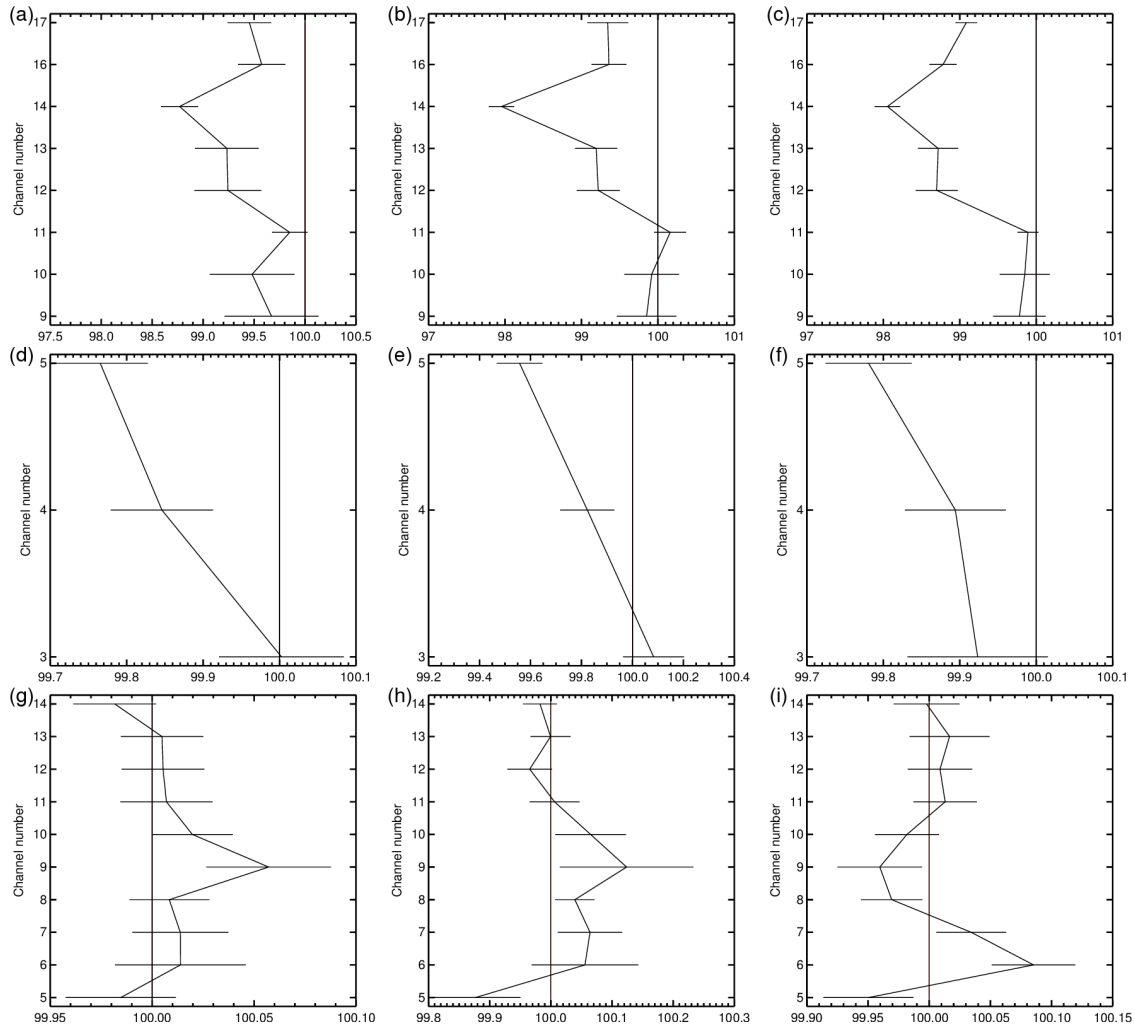


Figure 9: Normalized differences of the standard deviations of the FG departures in percentages. The normalization was performed against the Control run. Top panels are for SSMIS observations. (a) Northern hemisphere, (b) Tropics, and (c) Southern Hemisphere. Middle panels are for MHS observations. (d) Northern hemisphere, (e) Tropics, and (f) Southern Hemisphere. Bottom panels are for AMSU-A observations. (g) Northern hemisphere, (h) Tropics, and (i) Southern Hemisphere. Vertical axes indicate channel number. The error bars indicate a 95 % statistical confidence interval.

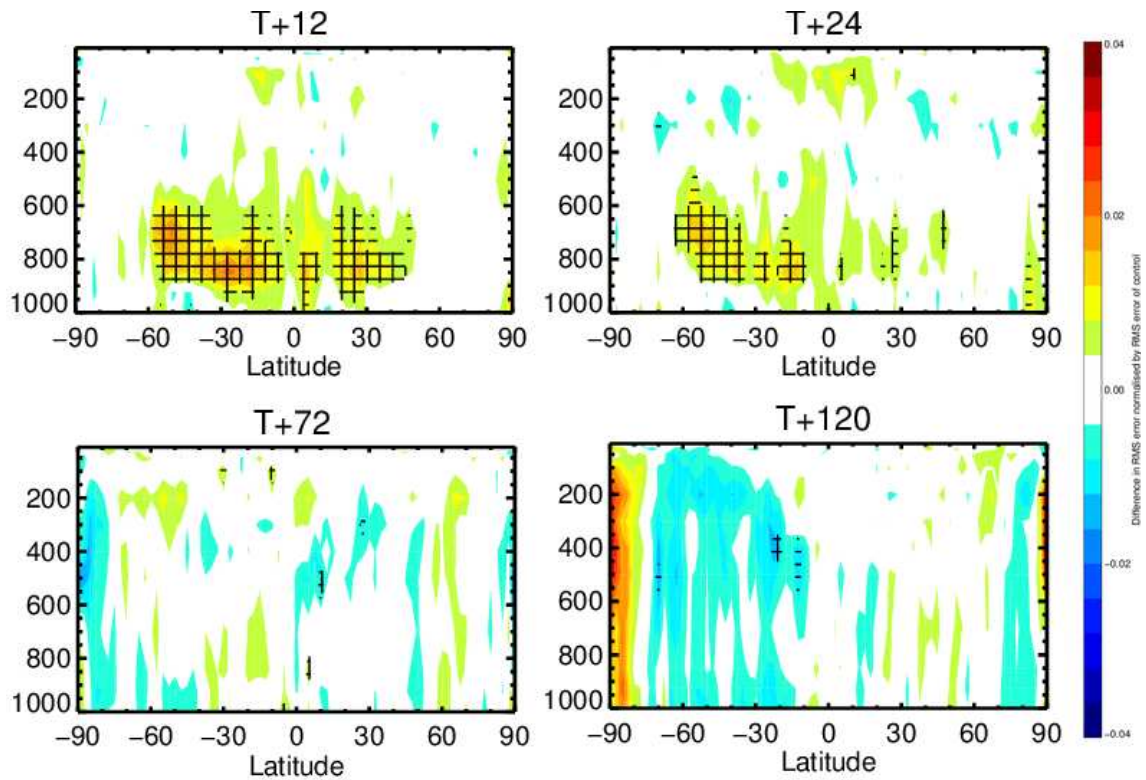


Figure 10: Normalized change in the RMS of vector wind forecast error between Test (AMS2 radiance are assimilated) and Control for 12, 24, 72, and 120 hour forecast. Blue areas indicate reduced RMS forecast errors and hence improved forecast; green/yellow/red areas indicate the opposite. Cross-hatched areas show changes that are significant at the 95 % confidence interval.

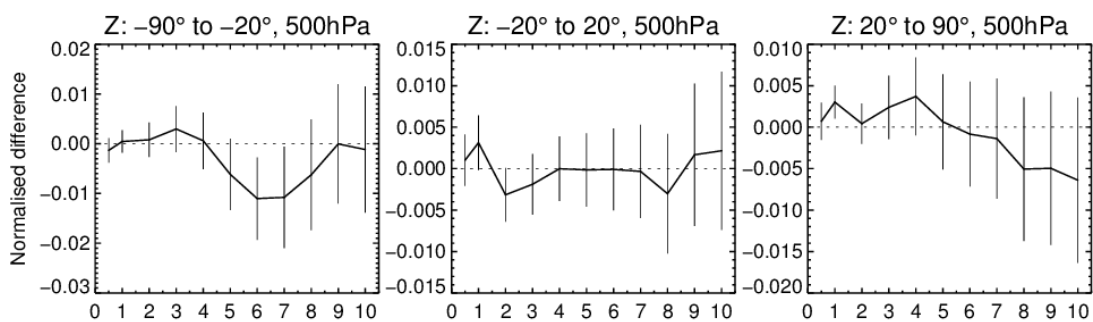


Figure 11: Normalized change in RMS forecast error in geopotential height at 500 hPa for the southern hemisphere, tropics, and northern hemisphere between Test (AMS2 assimilation) and Control. Horizontal axes indicate forecast day. Verification is against own analysis. The error bars indicate a 95 % statistical confidence interval.

quality of the humidity field in the FG is better than it is in the absence of SSMIS and TMI observations. When adding AMSR2 on top of the no-imager baseline, it makes much bigger changes to the humidity fields. However, in high latitude areas (around latitudes 60 degrees), relatively large changes of relative humidity remain in Test. Figure 12 (c) and (d) shows the temperature case. Although the size of the normalized change in RMS temperature error in the Tropics was reduced in Test, in the high latitudes (e.g. 40S to 60S), a similar size impact remains. In the wind fields ((e) and (f)), generally the changes are small in the Test compared to Test1. However, a large change in the East Pacific near the coast of the South America remains. As for geopotential height field ((g) and (h)), the pattern looks similar but the size is slightly smaller in the Test. Over the land, common improvements were found for these variables. The large changes in the short range are indicators of inconsistency between forecast model climate and observations. It could be forecast model biases or new observation information in the data assimilation. We must look in detail at the microwave imager's FG departure distribution for those areas.

4.3 Characteristics of microwave imagers FG departure bias

AMSR2 mean normalized FG departure distributions reveal biases that only occur under certain meteorological conditions. They seem to originate from issues in the forecast model and radiative transfer model performance. The spatial and temporal patterns of the biases are common among the microwave imagers. Figure 13 shows the mean normalized FG departures of assimilated AMSR2 radiances for 19GHz V and 37 GHz V channels. Similar biases exist in other channels. To examine characteristics of the biases, the FG departure data were separated for ascending data and descending data. This separation helps investigation on biases that are dependent on local time. We focus on the following three kinds of biases.

4.3.1 Biases in high surface wind speed and low wind direction variability areas

In Figure 13, the sign of the biases in the Arabian Sea (Somali jet) is different between the orbits although mean standard deviations of FG departure are smaller compared to other areas (Figure 14). As mentioned earlier, the effect of relative wind direction (i.e. the difference between surface wind direction and sensor azimuth angle) on ocean surface emissivity has not been modeled in these experiments. The biases in the Arabian Sea are caused by these issues, but they can be substantially reduced if the new RWD emissivity model of Kazumori and English (2014) is applied. This will be done in a future cycle of the IFS.

4.3.2 Biases in cold sectors

Positive and negative biases in high latitude areas in the southern hemisphere exist (Figure 15 (a)). The biases can be seen in both ascending and descending orbit data. Figure 15 (b) shows results of the quality control for a single day's data. Most of the positive biased data can be removed by the criteria (Eq. (6), (7), (8) and (9)).

Here we concentrate on the positive bias that seems to be occurring in the cold sectors near low pressure systems. The bias could come from known problems in mixed-phase Arctic cloud modeling (Klein et al., 2009). However, it is difficult to understand the real cause of this bias from only this figure. To show the cause of the bias, the dependency on atmospheric stability and surface wind speed were examined. As a measure of the atmospheric stability, air-sea temperature difference (2 m temperature minus surface temperature) was used. Figure 16 shows the results for AMSR2 channels. For these

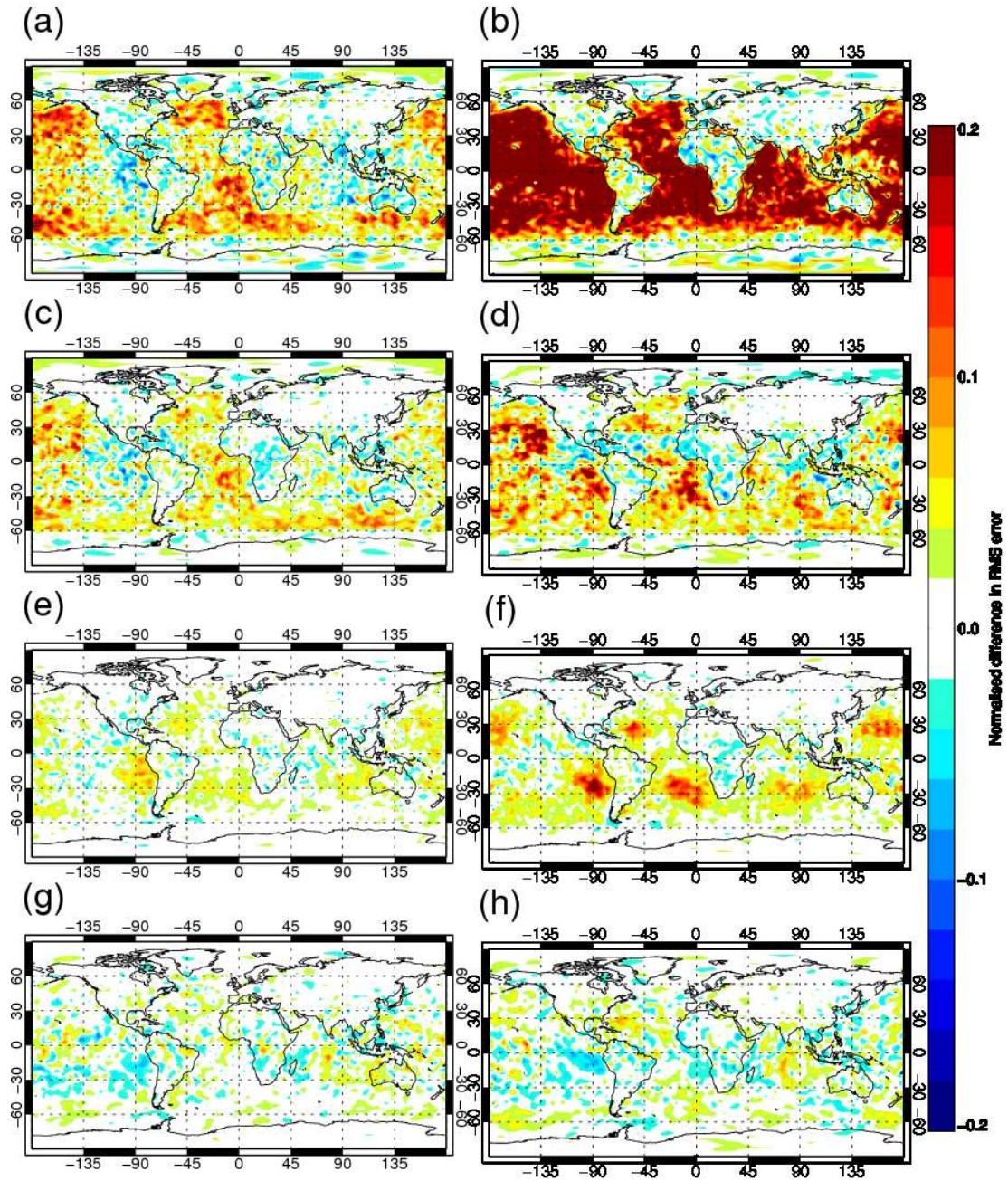


Figure 12: Normalized change in RMS errors at 12 hour forecasts. (a) relative humidity, (c) temperature, (e) vector wind, (g) geopotential height for Test run. The pressure levels are 850 hPa. (b), (d), (f), (h) are same but for Test 1 case. Both result from AMS2 assimilation but their experimental configuration is different.

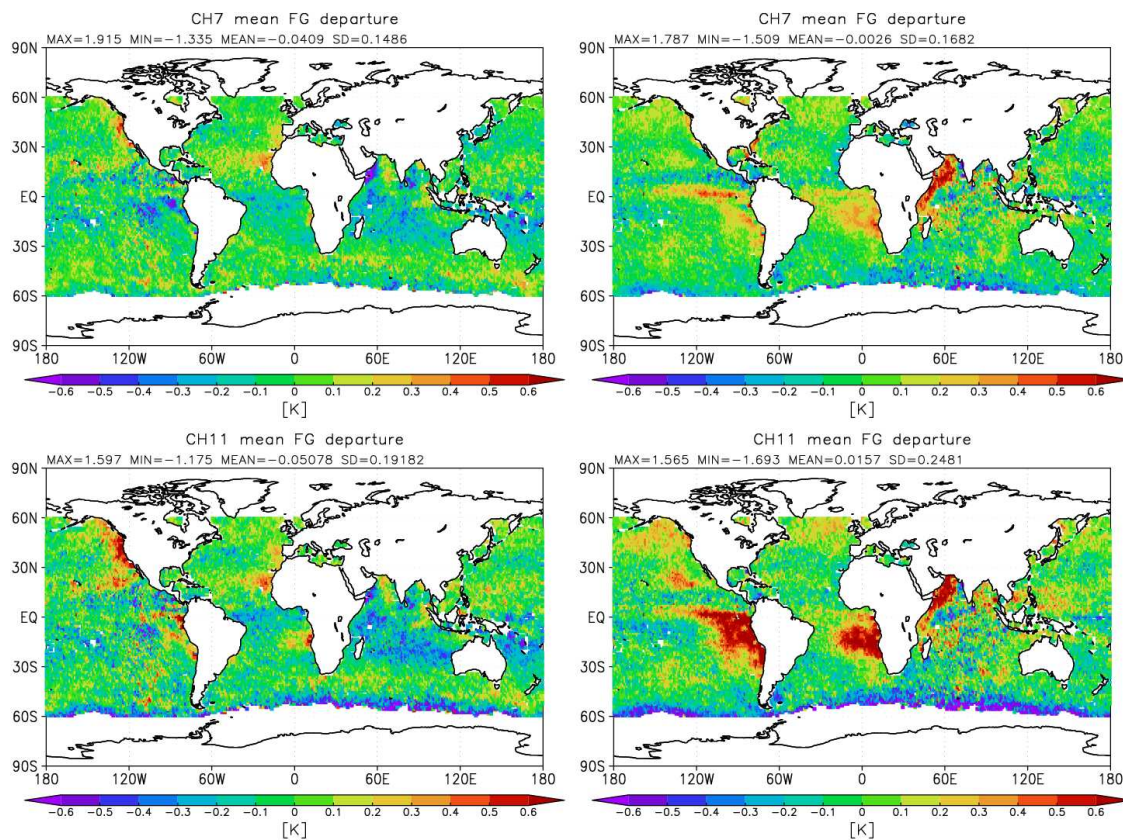


Figure 13: Normalized mean FG departure distributions of assimilated AMSR2 data in the Test. The period for the statistics is from 15 July to 15 October, 2013. Upper panels are AMSR2 19 GHz V, lower panels are 37 GHz V channels. The left panels indicate ascending orbit data (local time 13:30), the right panels indicate descending orbit data (local time 1:30).

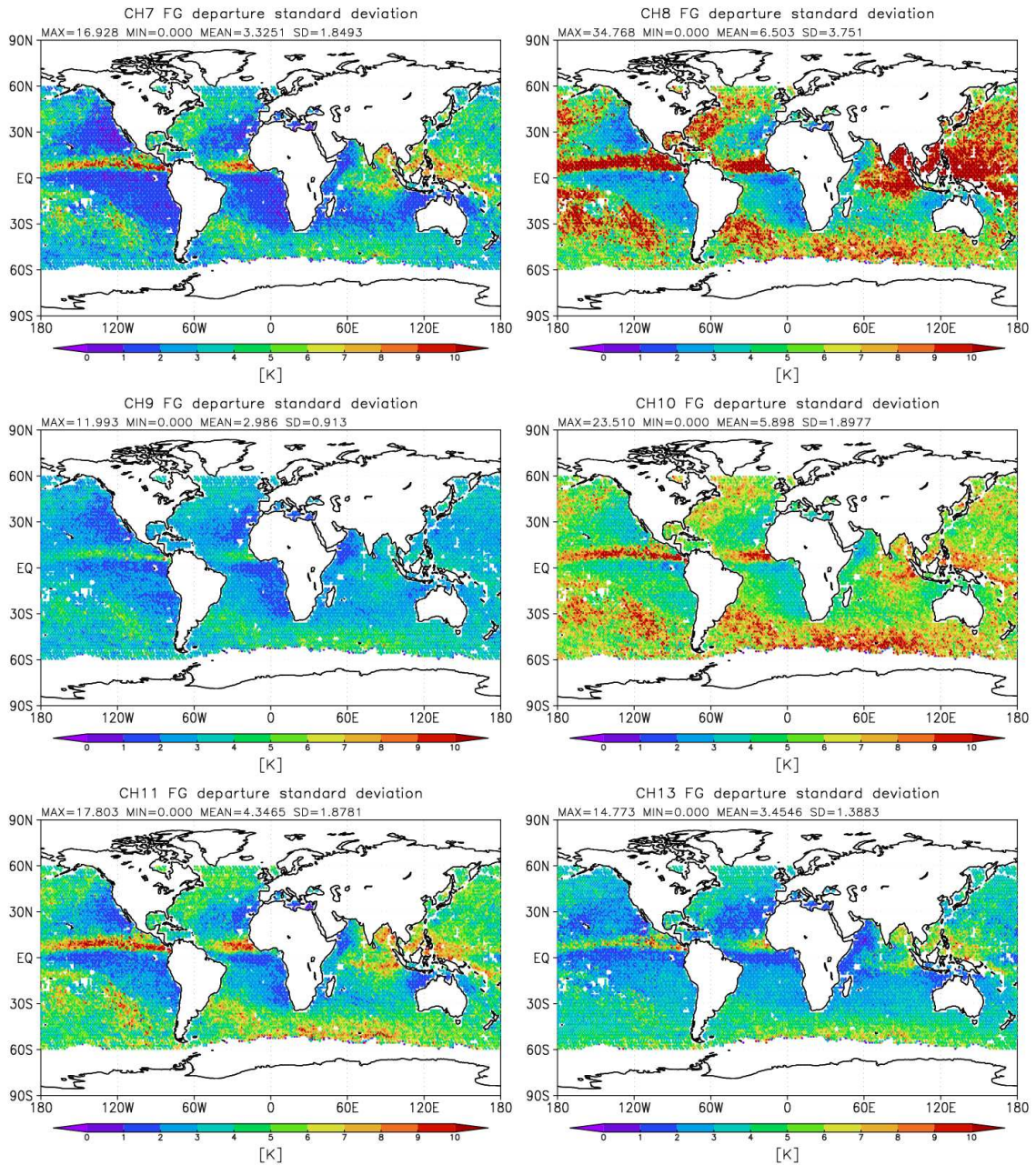


Figure 14: Standard deviations of AMSR2 FG departure used in the experiment. The statistic period is from 15 July to 15 October, 2013. Top left panel is 19 GHz V, top right is 19 GHz H, middle left is 23 GHz V, middle right is 23 GHz H, bottom left is 37 GHz V, and bottom right is 89 GHz V.

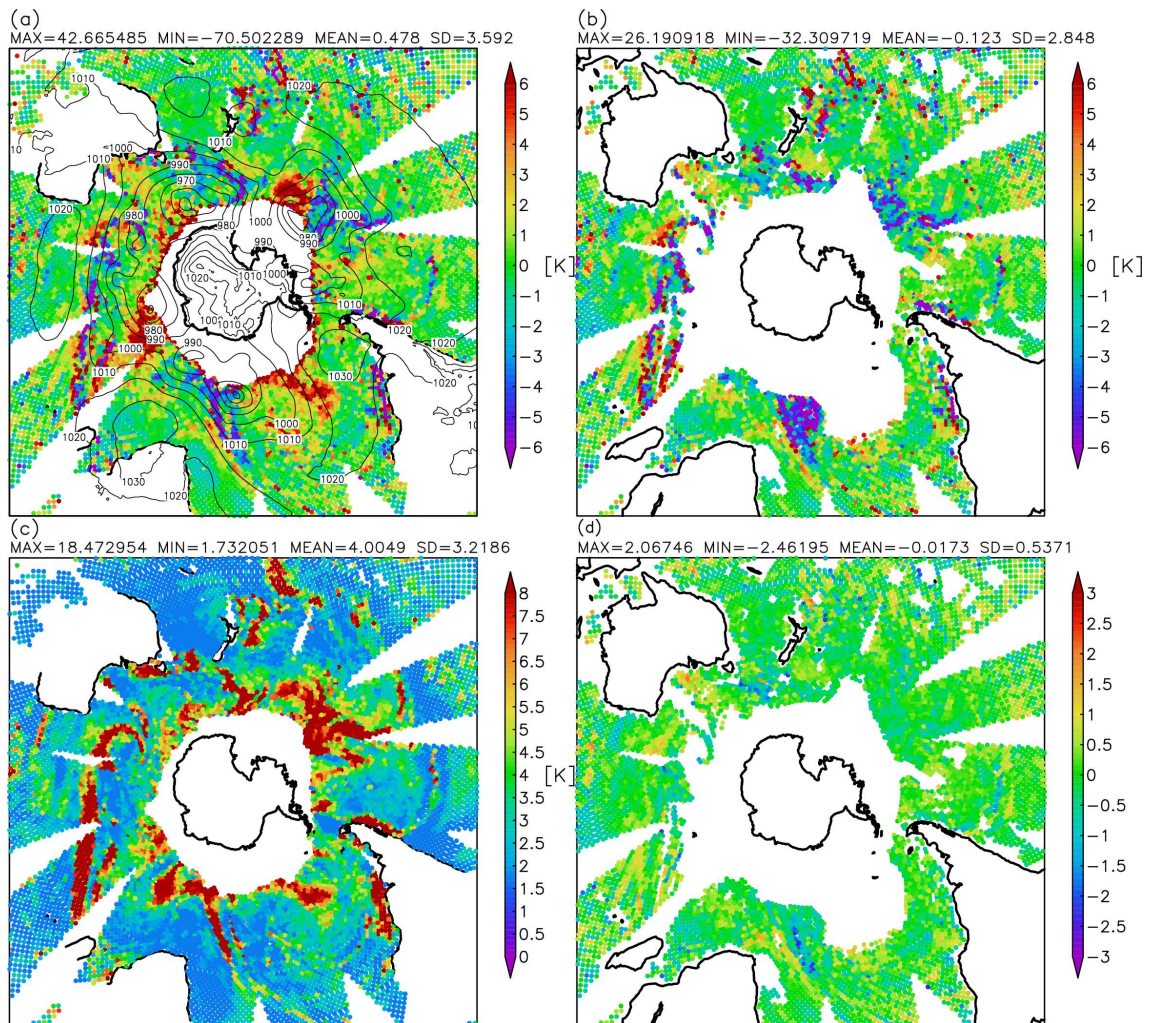


Figure 15: AMSR2 data distribution in the southern hemisphere on 30 September 2013. (a) 19 GHz VFG departure distribution from all ocean data. (b) Assimilated data. (c) Observation errors. (d) The normalized FGD departure.

statistics, passively monitored AMSR2 data for a long period (one year from August 2012 to July 2013) were used. The figure shows biases relative to those in neutral conditions (air sea temperature difference = 0) for each wind speed category. It is clear that the FG departures have negative correlation with air sea temperature difference at high surface wind speeds ($> 10 \text{ m s}^{-1}$). Larger positive biases can be seen in higher frequency channels. It suggests the biases are related to cloud signals in the observations. In cold sectors, insufficient cloud liquid water may be feature of the ECMWF forecast model. To confirm the assumption, AMSR2 cloud free data was plotted in Figure 17. The clear scene selection is based on NASA Moderate Resolution Imaging Spectroradiometer (MODIS) cloud product (Mantzel et al. 2002). Because AMSR2 on GCOM-W1 and MODIS on Aqua use the same afternoon orbit (A-Train), AMSR2 data can be matched up with the MODIS cloud product and the clear scenes can be selected. From comparison of Figure 16 and 17, it is clear that the positive biases occur mainly in cloudy conditions. Hence the biases are caused by insufficient LWP in the FG field. However, for low frequency channels (6 to 19 GHz, and horizontal channels), approximately 1.5 K positive biases exist for high surface wind and unstable conditions even under clear skies. This result suggests that some parts of the bias at high wind speeds are caused by surface emissivity modeling issues. In high surface wind speeds, foam and whitecap are generated by breaking waves. Unstable atmospheric conditions enhance the generation and the thickness of the foam and whitecap. Although the phenomenon of the increases in observed radiances under unstable conditions have been studied (Monahan and O’Muircheartaigh 1986, Reul and Chapron 2003, Shibata 2003, Shibata 2007, Wei 2013), no emissivity model is yet available that includes the effect of atmospheric stability on foam coverage.

To reduce the positive biases, the inclusion of the atmospheric stability effect in the ocean emissivity calculation and improvements of LWP representation in the FG field are necessary. However, the dominant part of the bias comes from insufficient LWP in the forecast model. In the data rejection for the biased data (Eq. (6), (7), (8), and (9)), the quality control rejects good data alongside bad data, as seen in Figure 15. Compared to the current quality control, the atmospheric stability (i.e. air sea temperature difference) and the surface wind speed could be better indexes for the detection of the biased data.

4.3.3 Positive biases in stratocumulus areas and their diurnal variations

Figure 13 shows clear positive biases west of the continents in the tropics. The biases are larger in descending orbits (night-time observations). These areas typically have large-scale marine stratocumulus clouds (Wood, 2012). The variability of the stratocumulus cloud shows LWP diurnal variations (Wood et al., 2002). The temporal and spatial variability of the cloud properties; i.e., LWP, cloud top height, and cloud thickness must be modeled correctly in general-circulation models (GCMs). Their radiative properties (i.e. reflection of incoming shortwave radiation with high albedo and emission of longwave radiation) affect Earth energy balance (Hartmann et al., 1992) and are one of the uncertainties in climate simulations (Bony et al., 2005). The amount of subtropical marine stratocumulus is usually underestimated in GCMs. Duynkerke and Teixeira (2001) showed that ECMWF Reanalysis (ERA) cloud cover and LWP are strongly underestimated.

The ECMWF all-sky assimilation system monitors the FG departures of microwave imagers on various sun-synchronous polar orbit satellites (AMSR2/GCOM-W1, SSMIS/DMSP F18, F17, F16, and WindSat/Coriolis) and one non sun-synchronous satellite (TMI/TRMM). Using these FG departure data, we are able to examine the model biases in the stratocumulus areas. The biases of the FG departure show a dependency on observation local time. Figure 18 and Figure 19, for the summer and winter cases, show the FG departure distributions of AMSR2 37 GHz V channel for areas characterized by marine stratocumulus, as well as for nearby areas where stratocumulus is uncommon. The bias in summer is

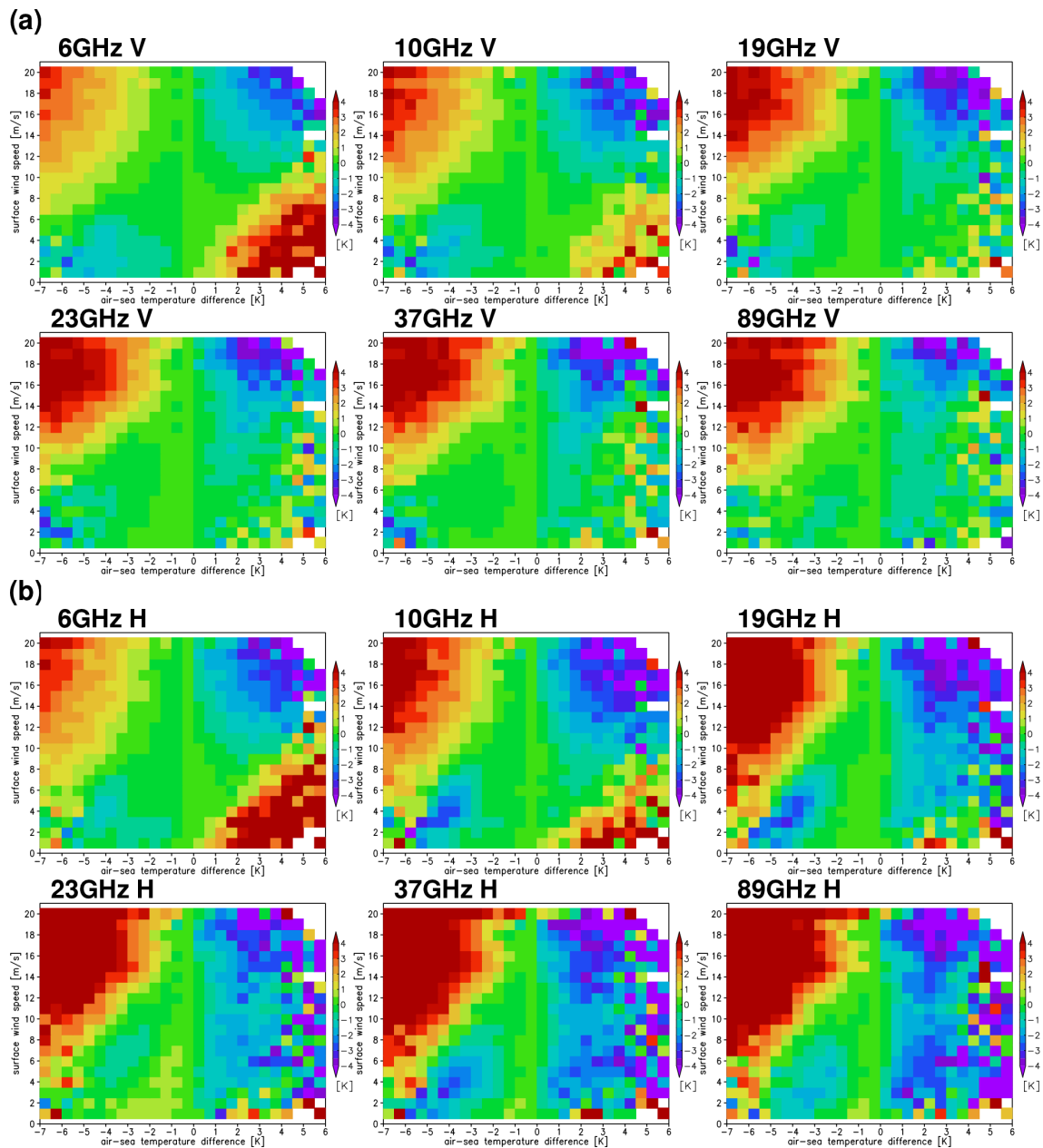


Figure 16: Mean AMSR2 FG departure as function of air sea temperature difference and surface wind speed under all sky condition. (a) AMSR2 vertical polarized channels (b) horizontal polarized channels. The statistic period is from August 2012 to July 2013.

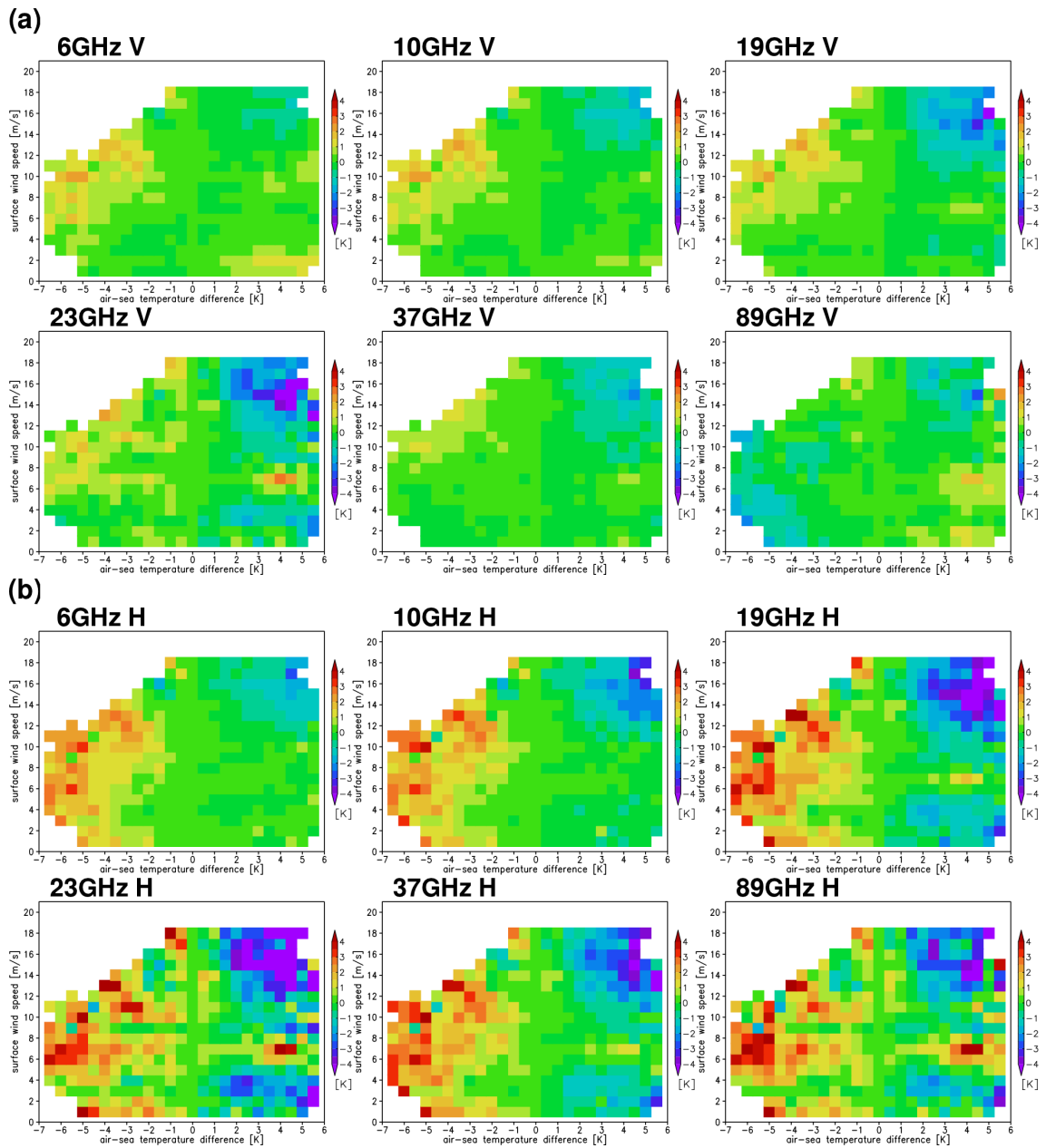


Figure 17: Same as Figure 16 but for clear sky condition data.

larger than that in winter cases. The biases tend to be limited to typical marine stratocumulus cloud areas. For the two areas referred to as (a), (b), Figure 18 (a), (b) and Figure 19 (a), (b) show the area averaged FG departure from the microwave imagers. Microwave imagers on polar orbiting satellites can provide two results per day. TMI can provide various local time statistics for the experiment period. The bias behavior in area (a) shows diurnal variation following the LWP amount itself. The bias variations were consistent among the microwave imagers, and could not be found in area (b). The biases in 19 GHz V and 23 GHz V channels are plotted for comparison as well. The biases in 37 GHz V are larger than those of other channels. Because 37 GHz channels have higher sensitivity to LWP than other channels, the results suggest LWP in the FG is underestimated in the night-time. In the stratocumulus areas, the data have smaller LWP amount than other areas and the standard deviation of the FG departure is also smaller as shown in Figure 14. Thus, the symmetric error model does not generate large observation errors in these regions, even though it would be desirable given the large biases. Figure 20 shows the variation of the cloud index C_{37} and the observed and FG cloud liquid water for TMI. The cloud liquid water observations are taken from the Remote Sensing Systems product. It is clear that the size of the LWP diurnal variation from the model is underestimated and the model's LWP amount is insufficient in the stratocumulus areas.

5 Discussion and Conclusion

In this study, the AMSR2 radiance data quality was evaluated and found to be comparable to other microwave imagers. Although the low frequency channels are affected by various kinds of RFI contamination, the channels selected for assimilation are less affected and prescreening with the observation model can reject most of the RFI contaminated data in AMSR2 19 GHz channels. The observation error model for AMSR2 was constructed based on the Geer and Bauer (2010, 2011) approach for all-sky assimilation.

To fairly compare the impact of the different microwave imagers in all-sky assimilation, experiments were performed where each instrument (AMSR2, SSMIS, and TMI) was added on top of a baseline without other microwave imagers. The results showed consistently improved FG fits to humidity sensitive observations for three microwave imagers. As for temperature sounding channels, degradations were found in some channels (AMSU-A channel 6, 9) though other channels were improved. Moreover, there were improved FG fits in wind and humidity observations. The three microwave imagers showed common positive impacts on analysis and forecasts. In the wind field forecast verification, large changes in RMS error were found at lower levels in the short range forecasts when using own-analyses as the verification reference. These resemble degradations in forecast quality, but they are not real degradations because the FG fit to observations is generally improved. In particular, the FG fit to AMV observations is improved by 1 % at similar levels, contradicting the own-analysis verification. The increased RMS differences in forecast minus own-analysis apparently results from new information provided by the microwave imagers. Moreover, significant improvements of wind and geopotential height fields in the troposphere were found in day 3 to day 6 forecasts. The improvements of the geopotential height forecasts by AMSR2 were larger than other microwave imagers in the northern hemisphere. Overall it would be beneficial to assimilate the AMSR2 radiance data.

With the addition of AMSR2 radiance data on top of the ECMWF operational dataset, mixed results were obtained. Consistent improvements in the FG fit to humidity observations were confirmed. However, degradations of the fit to several channels of microwave temperature sounding instruments and a worse fit to 200 hPa wind observations were found. The degradations might be caused by the biases observed in microwave imager data in certain local times and meteorological conditions. Because most of the

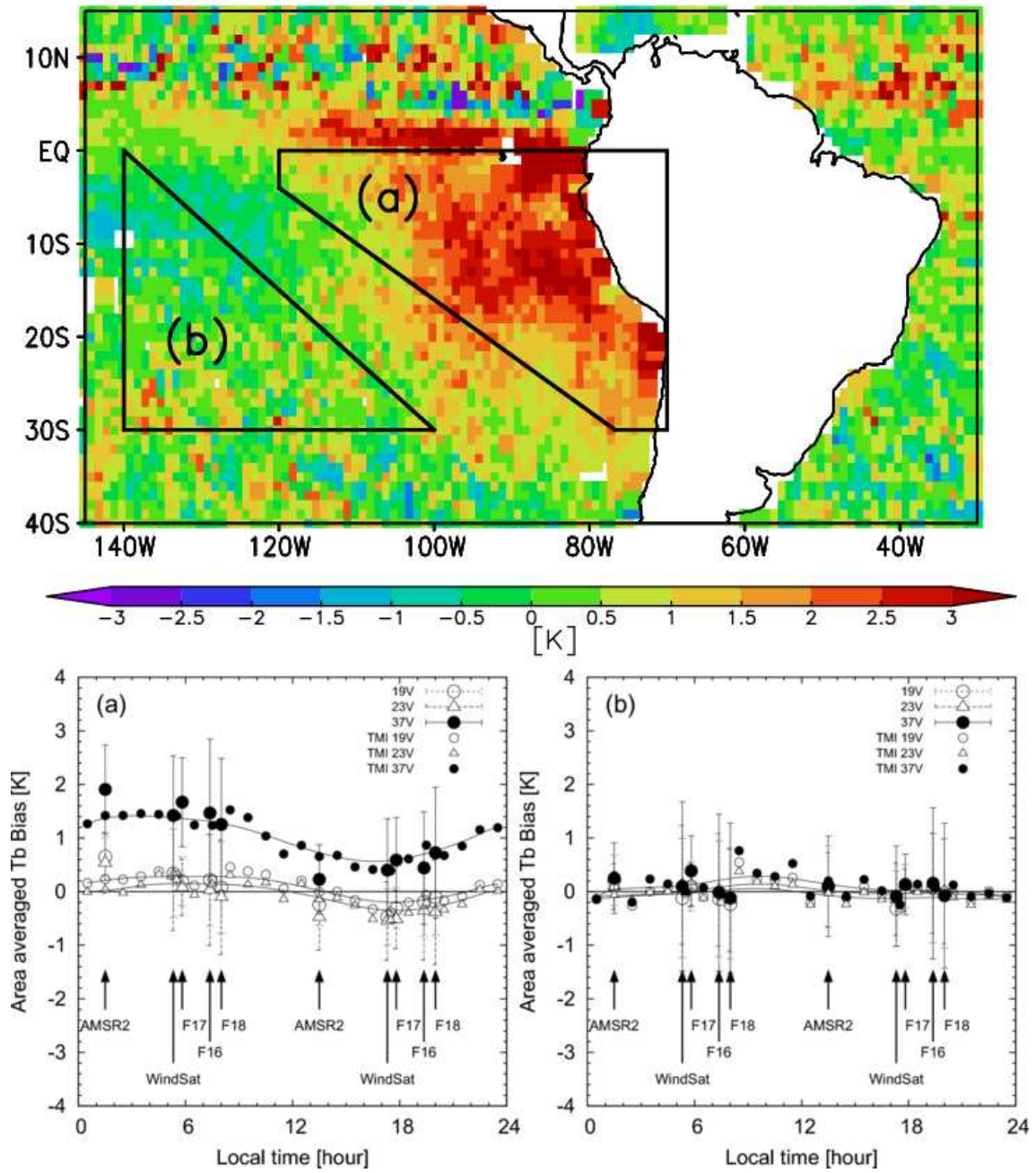


Figure 18: Area averaged FG departure biases in the summer experiment period. The area for averaging is plotted in top panel with AMSR2 37 GHz V mean FG departure map. The focused areas (a) and (b) are shown with surrounded area with black lines. Bottom panels show the biases as functions of observation local time of microwave imagers (AMSR2, SSMIS F16, F17, F18, WindSat, and TMI). TMI biases are shown with smaller symbols. White circle is 19 GHz V, white triangle is 23 GHz V, black filled circle is 37 GHz V biases. Bars indicate the standard deviations.

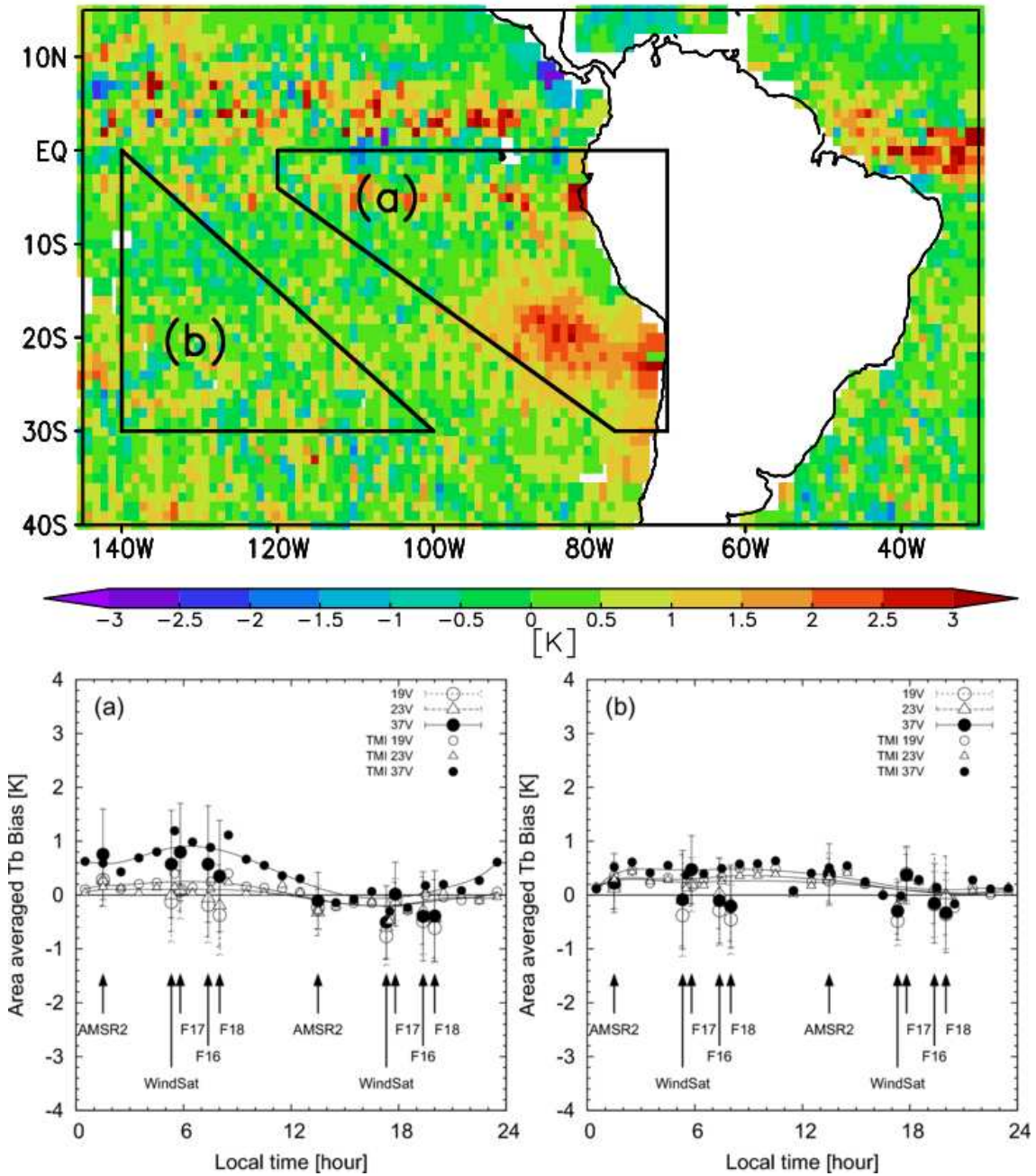


Figure 19: As Figure 18 but for the winter experiment period.

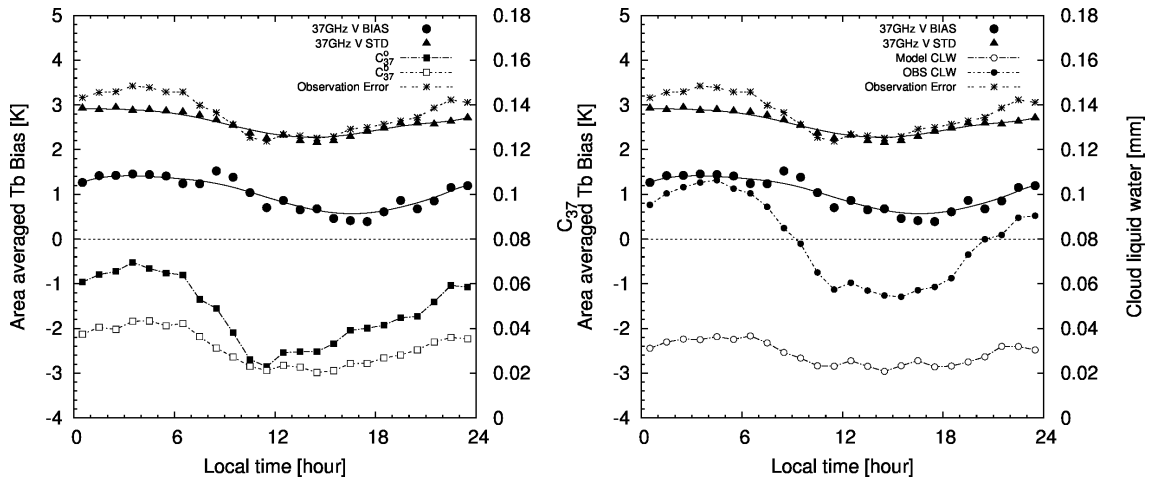


Figure 20: Mean diurnal variation of C_{37} (left panel) and cloud liquid water (right panel) for TMI in the summer experiment period at area (a). Observed cloud liquid water is products from Remote Sensing Systems. TMI 37 GHz V FG departure bias (black filled circle), standard deviation (black triangle), total errors (asterisk) are plotted in both panels.

benefits of the assimilation of the microwave imager radiances have already occurred with SSMIS and TMI radiances, there is less room for improvement when AMSR2 is added to the ECMWF system. In this scenario, the additional weight given to the biased data in the system (three imagers versus two imagers) might cause forecast deteriorations that outweigh the limited benefits of adding a third imager. However, adding AMSR2 radiance assimilation to the existing observing system still brought significant improvements in the geopotential height field in the southern hemisphere lower troposphere for day 5 to day 7 forecasts. It is hard to judge whether the improved medium range forecasts and better humidity analysis outweigh the small deteriorations in some observational FG fits. It is a finely balanced decision whether or not to add AMSR2 to the ECMWF operational assimilation.

The introduction of AMSR2 radiance data into the ECMWF system revealed cloud related forecast model performance issues. In the Test (addition of AMSR2 data to the operational dataset), additional increments in relative humidity were much smaller than those in Test 1 (AMSR2 data addition to the baseline). This indicates there is much less impact on humidity analyses when a third imager is added to a system where two imagers are already being assimilated. In contrast, the changes temperature increments remained of a similar order to those in Test 1 at high latitude areas. Current all-sky configuration does not fully reject these biased data and they are partially used in the assimilation (see Figure 15 (b)). The assimilation of these biased data could decrease analyzed cloud liquid water to improve consistency with the AMSR2 observations but at the same time they could cause spurious temperature and humidity increments. The negative effect might be one reason for degradations of the FG fit to AMSU-A channels and wind observations around the upper troposphere. As for AMSU-A channel 5, sensitive more to the lower troposphere, FG fits are improved significantly. However, the data selection for AMSU-A channel 5 limits its use to mainly clear scenes. Hence a change of analysis and FG quality in cloudy situations might not be observed in the AMSU-A channel 5 statistics. The same thing could be said for the results of the fits to infra-red sensors they are assimilated in clear conditions.

In tropics, it is confirmed that the positive biases in the FG departure depend on local time. Our examination on the FG departure biases using multiple polar orbiting satellites provided evidence of defects of the forecast model’s LWP diurnal variation representation. The LWP diurnal variation in the stra-

tocumulus areas is underestimated. The assimilation of the biased data might also bring negative effects coming from erroneous temperature increments and additional noise in the analysis and FG fields. It might explain the worse FG fit to some channels of AMSU-A in tropics. However, the degradation in tropics does not spread with forecast time. It remains in the same area and does not show any growth of the forecast errors. Microwave imagers observe the earth radiation from different orbits (i.e. they have different local times). Therefore, there is a possibility their assimilation impacts could be different where the forecast model and the radiative transfer model have issues that depend on local time or cloud development stages.

For more than two decades, microwave imager observations have been utilized in radiance data assimilation for NWP. The all-sky assimilation is a state-of-art approach in the microwave imager assimilation. It constrains the model physics including cloud physics and can find a balanced field of temperature, humidity, clouds, precipitation, and surface wind speed over oceans. Generally, all-sky assimilation works well with the ECMWF forecast model over the oceans. However, a basic assumption of data assimilation systems is that observations and model are unbiased relative to each other. This is not valid under certain meteorological conditions in the all-sky assimilation due to biases in cloud amounts in the forecast model. This study showed that there is still a lot of room for further improvement of the microwave imager data usage in cloud and rainy situation. Improvements in the cloud representation in the forecast model in high latitude cold sectors and in the tropics would likely bring substantial benefits to the quality of the all-sky assimilation.

Acknowledgements

This study was carried out under through a collaboration between ECMWF and Japan Meteorological Agency (JMA). This study was funded by a Fellowship Program by the Ministry of Education, Culture, Sports, Science and Technology of the Japanese Government. This work was supported by Global Change Observation Mission - Water1 (GCOM-W1) research with the Japan Aerospace Exploration Agency (JAXA) Earth Observation Research Center (EORC). The authors would like to thank Ioannis Mallas for AMSR2 data acquisition and conversion to BUFR format in the ECMWF system. The authors would like to thank Mieko Seki (Remote Sensing Technology Center of Japan) for providing the collocated AMSR2 and MODIS data through GCOM W1 research with JAXA EORC. TMI cloud liquid water data are produced by Remote Sensing Systems and sponsored by the NASA Earth Science MEaSURES DISCOVER Project. Data are available at www.remss.com.

References

- Andersson E, Järvinen H. 1998. ‘Variational quality control,’ Technical Memo. 250, 31pp. ECMWF: Reading, UK.
- Bauer P, Moreau E, Chevallier F, O’keefe U. 2006. Multiple-scattering microwave radiative transfer for data assimilation applications. *Q. J. R. Meteorol. Soc.* 132: 1259-1281. DOI:10.1256/qj.05.153
- Bauer P, Lopez P, Benedetti A, Salmond D, Moreau E. 2006a. Implementation of 1D+4D-Var assimilation of precipitation-affected microwave radiances at ECMWF. I: 1D-Var. *Q. J. R. Meteorol. Soc.* 132: 2270-2306.
- Bauer P, Lopez P, Salmond D, Benedetti A, Saarinen S, Moreau E. 2006b. Implementation of 1D+4D-Var

- assimilation of precipitation-affected microwave radiances at ECMWF. II: 4D-Var. *Q. J. R. Meteorol. Soc.* 132: 2307-2332.
- Bauer P, Geer AJ, Lopez P, Salmond D. 2010. Direct 4D-Var assimilation of all-sky radiances. Part I: Implementation. *Q. J. R. Meteorol. Soc.* 136: 1868-1885. DOI:10.1002/qj.659
- Bauer P, Auligne T, Bell W, Geer A, Guidard V, Heilliette S, Kazumori M, Kim M-J, Liu EH-C, McNally AP, Macpherson B, Okamoto K, Renshaw R, Riishjgaard L-P. 2011. Satellite cloud and precipitation assimilation at operational NWP centres. *Q. J. R. Meteorol. Soc.* 137: 1934-1951. DOI:10.1002/qj.905
- Bell W, Candy B, Atkinson N, Hilton F, Baker N, Bormann N, Kelly G, Kazumori M, Campbell W, Swadley S. 2008. The assimilation of SSMIS radiances in numerical weather prediction models. *IEEE Trans. Geosci. Remote Sensing* 46: 884-900.
- Bony S, Dufresne JL. 2005. Marine boundary layer clouds at the heart of tropical cloud feedback uncertainties in climate models. *Geophys. Res. Lett.* 32: DOI:10.1029/2005GL023851
- Bormann N, Geer AJ, Bauer P. 2011. Estimates of observation-error characteristics in clear and cloudy regions for microwave imager radiances from numerical weather prediction. *Q. J. R. Meteorol. Soc.* 137: 2014-2023. DOI:10.1002/qj.833
- Bormann N, Geer A, Wilhelmsson T. 2011. 'Operational implementation of RTTOV-10 in the IFS,' Technical Memo. 650, 23pp. ECMWF: Reading, UK.
- Bormann N, Geer A, English S. 2012. 'Evaluation of the microwave ocean surface emissivity model FASTEM-5 in the IFS,' Technical Memo. 667, 18pp. ECMWF: Reading, UK.
- Dee D. 2004. 'Variational bias correction of radiance data in the ECMWF system,' In Proceedings of workshop on assimilation of high spectral resolution sounders in NWP, 28 Jun. - 1 Jul. 2004. ECMWF: Reading, UK. <http://www.ecmwf.int>
- Desroziers G, Berre L, Chapnik B, Poli P. 2005. Diagnosis of observation, background and analysis-error statistics in observation space. *Q. J. R. Meteorol. Soc.* 131: 3385-3396. DOI:10.1256/qj.05.108
- Duynkerke PG, Teixeira J. 2001. Comparison of the ECMWF reanalysis with FIRE I observations: Diurnal variation of marine stratocumulus. *J. Climate.* 14: 1466-1478.
- English S, McNally T, Bormann N, Salonon K, Matricardi M, Horanyi A, Rennie M, Janisková M, Michele SD, Geer A, Tomaso ED, Cardinali C, Rosnay P, Sabater JM, Bonavita M, Albergel C, Engelen R, Thépaut JN. 2013. 'Impact of satellite data,' Technical Memo. 711, 46pp. ECMWF: Reading, UK.
- Geer AJ, Bauer P, O'Dell CW. 2009. A revised cloud overlap scheme for fast microwave radiative transfer in rain and cloud. *J. App. Meteor. Clim.* 48: 2257-2270. DOI:10.1175/2009JAMC2170.1
- Geer AJ, Bauer P, Lopez P. 2010. Direct 4D-Var assimilation of all-sky radiances. Part II: Assessment. *Q. J. R. Meteorol. Soc.* 136: 1886-1905. DOI:10.1002/qj.681
- Geer AJ, Bauer P. 2010. 'Enhanced use of all-sky microwave observations sensitive to water vapour, cloud and precipitation,' Technical Memo. 620, 41pp. ECMWF: Reading, UK.
- Geer AJ, Bauer P. 2011. Observation errors in all-sky data assimilation. *Q. J. R. Meteorol. Soc.* 137: 2024-2037. DOI:10.1002/qj.830
- Geer AJ. 2013. 'All-sky assimilation: better snow-scattering radiative transfer and addition of SSMIS humidity sounding channels,' Technical Memo. 706, 26pp. ECMWF: Reading, UK.

- Geer AJ, Baordo F. 2014. Improved scattering radiative transfer for frozen hydrometeors at microwave frequencies. *Atmos. Meas. Tech. Discuss.*, 7, 1749-1805. DOI:10.5194/amtd-7-1749-2014
- Hartmann DL, Ockert-Bell ME, Michelson ML. 1992. The effect of cloud type on Earth's energy balance: Global analysis. *J. Climate*. 5: 1281-1304.
- Imaoka K, Kachi M, Fujii H, Murakami H, Hori M, Ono A, Igarashi T, Nakagawa K, Oki T, Honda Y, and Shimoda H, Global Change Observation Mission (GCOM) for monitoring carbon, water cycles, and climate change, *Proceedings of the IEEE*, vol. 98, no. 5, pp. 717-734, 2010.
- Ingleby NB, Lorenc AC. 1993. Bayesian quality control using multivariate normal distributions. *Q. J. R. Meteorol. Soc.* 119: 1195-1225.
- JAXA. 2013. GCOM-W1 SHIZUKU Data Users Handbook. First edition. Japan Aerospace Exploration Agency.
- Järvinen H, Undén P. 1997. 'Observation screening and background quality control in the ECMWF 3D Var data assimilation system,' Technical Memo. 236, 33pp. ECMWF: Reading, UK.
- Joseph J, Wiscombe WJ, Weinman JA. 1976. The delta-Eddington approximation for radiative flux transfer. *J. Atmos. Sci.* 33: 2452-2459.
- Kasahara M, Imaoka K, Kachi M, Fujii H, Naoki K, Maeda T, Ito N, Nakagawa K, and Oki T. 2012. Status of AMSR2 on GCOM-W1, *Proc. SPIE 8533, Sensors, Systems, and Next-Generation Satellites XVI*, 853307 (November 19, 2012). doi:10.1117/12.975810.
- Kawanishi T, Sezai T, Ito Y, Imaoka K, Takeshima T, Ishido Y, Shibata A, Miura M, Inahata H, Spencer R. 2003. The Advanced Microwave Scanning Radiometer for the Earth Observing System (AMSR-E), NASDA's contribution to the EOS for global energy and water cycle studies. *IEEE Trans. Geosci. Remote Sensing*. 41: 184-194.
- Kazumori M. 2014. Satellite radiance assimilation in the JMA operational mesoscale 4DVAR system. *Mon. Weather Rev.* 142: 1361-1381.
- Kazumori M, Egawa T. 2014. Assimilation of GCOM-W1/AMSR2 radiance data in the JMA NWP systems. *WGNE Blue book: Research Activities in Atmospheric and Ocean Modelling, WMO/Working Group on Numerical Experimentation*. 1. 07-08.
- Kazumori M, English SJ. 2014. Use of the ocean surface wind direction signal in microwave radiance assimilation. *Q. J. R. Meteorol. Soc.* in press. DOI:10.1002/qj.2445
- Kazumori M, Liu Q, Treadon R, Derber JC. 2008. Impact study of AMSR-E radiances in the NCEP global data assimilation system. *Mon. Weather Rev.* 136: 541-559. DOI:10.1175/2007MWR2147.1
- Klein SA, McCoy RB, Morrison H, Ackerman AS, Avramov A, Boer Gd, Chen M, Cole JNS, Del Genio AD, Falk M, Foster MJ, Fridlind A, Golaz JC, Hashino T, Harrington JY, Hoose C, Khairoutdinov MF, Larson VE, Liu X, Luo Y, McFarquhar GM, Menon S, Neggers RAJ, Park S, Poellot MR, Schmidt JM, Sednev I, Shipway BJ, Shupe MD, Spangenberg DA, Sud YC, Turner DD, Veron DE, Salzen KV, Walker GK, Wang Z, Wolf AB, Xie S, Xu KM, Yang F, Zhang G. 2009. Intercomparison of model simulations of mixed-phase clouds observed during the ARM Mixed-Phase Arctic Cloud Experiment. I: single-layer cloud. *Q. J. R. Meteorol. Soc.* 135: 979-1002. DOI:10.1002/qj.416
- Kummerow C, Barnes W, Kozu T, Shiue J, Simpson J. 1998. The Tropical Rainfall Measuring Mission (TRMM) sensor package. *J. Atmos. Ocean. Tech.* 15: 809-817.

- Kunkee DB, Poe GA, Boucher DJ, Swadley SD, Hong Y, Wessel JE, Uliana EA. 2008. Design and evaluation of the first Special Sensor Microwave Imager/Sounder. *IEEE Trans. Geosci. Remote Sensing* 46: 863-883.
- Liu Q, Weng F, English SJ. 2011. An improved fast microwave water emissivity model. *IEEE Trans. Geosci. Remote Sensing* 49: 1238-1250. DOI:10.1109/TGRS.2010.2064779
- Menzel WP, Baum BA, Strabala KA, Frey RA. 2002: Cloud Top Properties and Cloud Phase - Algorithm Theoretical Basis Document. NASA. ATBD Reference Number: ATBD-MOD-04.
- Monahan EC, O'muircheartaigh IG. 1986. Whitecaps and the passive remote sensing of the ocean surface. *Int. J. Remote Sensing*, 7: 627-642.
- Petty G, Katsaros K. 1990. Precipitation observed over the South China Sea by the Nimbus-7 Scanning Multichannel Microwave Radiometer during Winter MONEX. *J. Appl. Meteorol.* 20: 273-287.
- Petty G. 1994. Physical retrievals of over-ocean rain rate from multichannel microwave imagery. Part I: Theoretical characteristics of the normalized polarization and scattering indices. *Meteorol. Atmos. Phys.* 54: 79-99.
- Reul N, Chapron B. 2003. A model of sea-foam thickness distribution for passive microwave remote sensing applications. *J. Geophys. Res.* 108: DOI:10.1029/2003JC001887
- Saunders R, Matricardi M, Brunel P. 1999. An improved fast radiative transfer model for assimilation of satellite radiance observations. *Q. J. R. Meteorol. Soc.* 125: 1407-1425.
- Saunders R, Hocking J, Rayer P, Matricardi M, Geer A, Bormann N, Brunel P, Karbou F, Aires F. 2010. 'RTTOV-10 Science and validation report,' NWPSAF-MO-TV-023, v1.11, 1-31, EUMETSAT NWP-SAF.
- Shibata A. 2003. A change of microwave radiation from the ocean surface induced by air-sea temperature difference. *Radio Sci.* 38: 8063. DOI:10.1029/2002RS002670
- Shibata A. 2007. Effect of air-sea temperature difference on ocean microwave brightness temperature estimated from AMSR, SeaWinds, and BuOys. *J. Oceanography.* 63: 863-872.
- Treadon RE, Pan HL, Wu WS, Lin Y, Olson WS, Kuligowski RJ. 2002. Global and regional moisture analysis at NCEP. In Proc. Workshop on Humidity Analysis, Reading, United Kingdom. ECMWF: Reading, UK; pp 33-47.
- Wei EB. 2013. Effective medium approximation model of sea foam layer microwave emissivity of a vertical profile. *Int. J. Remote Sens.* 34: 1180-1193. DOI:10.1080/01431161.2012.718461
- Wood R, Bretherton C, Hartmann DL. 2002. Diurnal cycle of liquid water path over the subtropical and tropical oceans. *Geophys. Res. Lett.* 29: DOI:10.1029/2002GL015371
- Wood R. 2012. REVIEW Stratocumulus Clouds. *Mon. Weather Rev.* 140: 2373-2423. DOI:10.1175/MWR-D-11-00121.1